Conformation Selection by ATP-competitive Inhibitors and Allosteric Communication in ERK2

Jake W. Anderson[1], David Vaisar[1], David N. Jones[2], Laurel M. Pegram[1,4], Huifen Chen[3], John G. Moffat[3], and Natalie G. Ahn[1,5]

[1] Department of Biochemistry, University of Colorado, Boulder, CO; [2] Department of Pharmacology, University of Colorado Anschutz Medical Center, Aurora, CO, and [3] Genentech, Inc. South San Francisco, CA, USA

[4] Present address: Loxo Oncology, Louisville, CO 80027

[5] Corresponding author: Natalie Ahn, Department of Biochemistry, University of Colorado, Boulder, CO 80309; Phone: 303-492-4799; Email: natalie.ahn@colorado.edu

ABSTRACT

Activation of the extracellular signal regulated kinase-2 (ERK2) by phosphorylation has been shown to involve changes in protein dynamics, as determined by hydrogen-deuterium exchange mass spectrometry (HDX-MS) and NMR relaxation dispersion measurements. These can be described by a global exchange between two conformational states, named “L” and “R”, where R is associated with a catalytically productive ATP-binding mode. An ATP-competitive ERK1/2 inhibitor, Vertex-11e, has properties of conformation selection for the R-state, revealing movements of the activation loop that are allosterically coupled to the kinase active site. However, the features of inhibitors important for R-state selection are unknown. Here we survey a panel of ATP-competitive ERK inhibitors using HDX-MS and NMR and identify 14 new molecules with properties of R-state selection. They reveal effects propagated to distal regions in the P+1 and helix αF segments surrounding the activation loop, as well as helix αL16. Crystal structures of inhibitor complexes with ERK2 reveal systematic shifts in the Gly loop and helix αC, mediated by a Tyr-Tyr ring stacking interaction and the conserved Lys-Glu salt bridge. The findings suggest a model for the R-state involving small movements in the N-lobe that promote compactness within the kinase active site and alter mobility surrounding the activation loop. Such properties of conformation selection might be exploited to modulate the protein docking interface used by ERK substrates and effectors.

Keywords: ERK2, MAP kinase, inhibitor, conformation selection, NMR, hydrogen-deuterium exchange, cancer therapeutics

INTRODUCTION

The extracellular signal-regulated protein kinases, ERK1/2, are key components of the MAP kinase signaling pathway controlling cell proliferation, survival, morphology, and migration (Lavoie et al., 2020; Roskoski, 2012; Plotnikov et al., 2010). Due to the prevalence of oncogenic mutations in Ras, RAF and MEK, components of this pathway have been targeted for the development of successful anti-cancer therapies (Halle and Johnson, 2021; Tangella et al., 2021; Canon et al., 2019; Ryan et al., 2020). Although inhibitors targeting ERK1/2 have not advanced to clinical use, clinical trials are ongoing for several, including ulixertinib/BVD523 (Biomed Valley Diagnostics), ravoxertinib/GDC0994 (Genentech), and tizakertib/ATG017/AZD0364 (Antengene), for the treatment of cancers with activating mutations in KRAS, BRAF, NRAS, MEK1/2 and ERK1/2 (Grierson et al., 2023; Goodwin et al., 2023; Wu et al., 2021; Varga et al., 2019; Kong et al., 2023; Chen et al., 2021). Importantly, reversible ATP-competitive inhibitors targeting ERK1/2 have been shown to be effective in cancer cells and tumors with acquired resistance to BRAF and MEK inhibitors (Ryan et al., 2015; Morris et al., 2013; Hatzivassiliou et al., 2012; Roskoski et al., 2019; Pan et al., 2022). Therefore, future anticancer drug development would benefit from a more complete understanding of the properties of ERK inhibitors.

Many protein kinases undergo relatively large conformational changes when they switch from inactive to active states. Such changes lead to repositioning of conserved active site residues, including a Lys-Glu salt bridge in the N-terminal lobe between strand β3 and helix αC that hydrogen bonds with nucleotide phosphate, an Asp residue in the DFG motif that coordinates Mg^{2+}, and an Asp in the HRD motif that catalyzes base-assisted phosphoryltransfer to the substrate hydroxyl acceptor (Taylor et al., 2019; Amatya et al, 2019). By contrast, ERK2 is unusual in that only small conformational changes occur within the active site between the inactive, unphosphorylated (0P) and the active, dual phosphorylated (2P) forms of the kinase (**Suppl. Fig. S1**). X-ray structures show that phosphorylation of ERK2 at T183 and Y185 remodels the activation loop by forming phosphate salt bridges with several Arg residues (Zhang et al., 1994; Canagarajah et al., 1997). This accommodates the S/T-P recognition motif common to ERK substrates and exposes a pocket for binding a hydrophobic docking motif found in substrates, scaffolds and other effectors (Lee et al., 2004). But within the ATP binding site, the conserved residues that form the K52-E69 salt bridge, the DFG metal binding site (D165), and the HRD catalytic base (D147) are largely overlapping. Thus, the changes in the active site that accompany ERK2 activation are small and difficult to discern crystallographically.

Solution measurements revealed that the activation of ERK2 is accompanied by changes in protein dynamics. NMR Carr-Purcell-Meiboom-Gill (CPMG) relaxation dispersion measurements showed that phosphorylation results in a global exchange behavior that can be modeled by two conformational states, named “R” and “L”, which exchange on a millisecond timescale (Xiao et al., 2014, 2015; Iverson et al., 2020). Whereas the L-state resembles that seen with 0P-ERK2, the R-state appears only in 2P-ERK2, where it exchanges with an R:L population ratio of 80:20 at 25°C. Crystal structures of nucleotide-bound 0P- and 2P-ERK2 show significant differences. In 2P-ERK2, the ATP analog, AMP-PNP, is positioned close to the catalytic base and in-line for nucleophilic attack to the Pγ phosphate (Pegram et al., 2019; Lechtenberg et al., 2017). By contrast, ATP bound to 0P-ERK2 is markedly distorted, moving Pγ away from the base by more than 6 Å (Zhang et al., 2012; Smorodinsky et al., 2016). Thus, despite the structural similarity between the apoenzymes, 2P-ERK2 promotes ATP binding interactions that are more productive for catalytic function. The unique appearance of the R-state in 2P-ERK2 has been proposed to confer this ability (Pegram et al., 2019).

Interestingly, ATP competitive inhibitors of ERK show properties of conformation selection, where ligand binding traps conformational states in 2P-ERK2 that normally undergo reversible exchange in the apoenzyme. Binding of the inhibitor, Vertex-11e (VTX11e), to 2P-ERK2 shifts the L⇌R equilibrium completely to the R-state, while the inhibitor SCH772984 shifts the equilibrium completely to the L-state (Rudolph et al., 2015; Pegram et al., 2019). Conformation selection is absent in the inhibitor, GDC0994, where R and L retain a population ratio similar to that seen in the apoenzyme (Pegram et al., 2019). This selective recognition could explain why the binding of VTX11e is 10-fold stronger to 2P-ERK2 than 0P-ERK2 (Rudolph et al., 2015). In contrast, GDC0994 and SCH772984 bind both active and inactive kinase forms with equal affinity (Pegram et al., 2019; Ward et al., 2019).

Hydrogen-deuterium exchange mass spectrometry (HDX-MS) also reveals differences between VTX11e, GDC0994 and SCH772984 in their ability to induce perturbations at the P+1 segment (Pegram et al., 2019). P+1 is distal to the kinase active site, and along with the activation loop forms part of the interface for substrate and effector binding. This suggests that R⇌L conformational shifts within the active site can propagate out to the activation loop and surrounding regions. NMR-CPMG measurements confirm that activation loop residues participate in the same global exchange motion as residues surrounding the active site. Therefore, solution

measurements of conformation selective inhibitors shows that occupancy at the active site are allosterically coupled to distal movements at and surrounding the activation loop.

A consequence of this behavior is that conformation selective inhibitors can alter the interactions of ERK2 with other proteins. For example, binding of VTX11e partially inhibits the rate of dephosphorylation at the activation loop by the MAP kinase phosphatase, MKP3/DUSP6, while SCH772984 enhances this rate. The features of VTX11e controlling its property of R-state selection are unknown. An attempt to address this compared crystal structures of complexes formed between 2P-ERK2 and VTX11e (100% R), GDC0994 (80% R), or SCHCPD336, a close analog of SCH772984 (0% R) (Pegram et al., 2019; Chaikuad et al., 2014; Blake et al., 2016). But the results were inconclusive. Binding of SCHCPD336 disrupted Gly loop and helix αC interactions leading to a disordered activation loop, suggesting that the L state might communicate N-lobe deformities to the activation loop dynamics. In contrast, VTX11e and GDC0994 formed similar close contacts with active site residues with no major distortions in the ATP pocket. Given the limited set of compounds with small structural differences, it was difficult to identify features of binding that could explain R-state selection by VTX11e but not GDC0994.

Here we survey a panel of small molecules with varying chemical scaffolds, using HDX-MS and NMR to classify their properties of conformation selection. Of 19 inhibitors examined, 14 behave in a similar manner to VTX11e, with conformational selection for the R state. These include 13 novel inhibitors and ulixertinib/BVD523, a promising ERK inhibitor with blood brain barrier permeability (Sullivan et al., 2018; Yu et al., 2022; Siguad et al., 2023). Four inhibitors resemble GDC0994 in allowing R⇌L exchange with populations comparable to apoenzyme, and one allows exchange but partially shifts the equilibrium towards the R-state. NMR chemical shifts reveal perturbations unique to R-state inhibitors located in the P+1 segment and helix αL16, and remote from the inner-sphere region of ligand contact. Co-crystal structures of R-state selective inhibitors complexed with ERK2 show small but systematic conformational shifts in the Gly loop, helix αC and helix αL16, in which the Gly loop moves closer to the DFG segment, while helices αC and αL16 shift outwards. This movement rotates the N- and C-lobes into a more closed configuration and moves the K52-E69 salt bridge closer to the conserved DFG motif. Such small but systematic conformational shifts suggest a working model for R-state selection, involving movements of the N-lobe that favor a more compact active site with allosteric coupling to the activation loop.

RESULTS

Solution measurements reveal R-state conformation selection.

NMR experiments were used to examine conformation selection by inhibitor binding. Previously, NMR-CPMG measurements of ERK2, selectively [methyl-^{1}H,^{13}C]-labeled on Ile, Leu and Val (ILV) residues, showed that phosphorylation introduced global motions involving multiple residues in the N- and C-lobes surrounding the active site, as well as in the activation loop (Xiao et al., 2014; Iverson et al., 2020). These could be modeled by a global two-state exchange process (R⇌L) with exchange rate constant k_{ex} = 300 s^{-1}. As shown previously (Xiao et al., 2014, Iverson et al., 2020), the R:L populations were 80:20 at 25°C and 50:50 at 5°C for the 2P-ERK2 apoenzyme, and 0:100 for the 0P-ERK2 apoenzyme at both 25°C and 5°C.

NMR spectroscopy was used to test the effect of inhibitors on conformational exchange in 2P-ERK2. BVD523 shares chemical features with VTX11e including a central amido-linked pyrrole scaffold (**Fig. 1A**). **Fig. 1B-D** illustrates methyl probes with slow exchange ($\Delta\omega >> k_{ex}$), allowing the relative populations of R and L separated by their chemical shift differences to be observed in 2D (^{1}H,^{13}C)-HMQC spectra. Saturation binding of BVD523 shifted the R⇌L equilibrium to 100% R at both 25°C and 5°C, matching the effects of VTX11e (**Fig. 1B-D**). In contrast, GDC0994 had little effect on the R and L populations relative to apoenzyme (**Fig. 1B-D**). The results show that BVD523, like VTX11e, exhibits properties of R-state conformational selection. This behavior might explain why BVD523 preferentially binds the activated kinase, with ~10-fold higher affinity for 2P-ERK2 than 0P-ERK2 (Germann et al., 2017).

HDX-MS experiments were conducted as a complementary approach to compare the effects of BVD523 to VTX11e and GDC0994 on conformational selection (**Suppl. Dataset S1**). Binding of all three inhibitors reduced deuteration at conserved regions in the active site, including the Gly-rich loop, helix αC, the hinge and helix αE, to a comparable degree between 0P- and 2P-ERK2 (**Fig. 2A-C**, light green; **Suppl. Figs. S2**, **S3**, **S4**). All three inhibitors also reduced HDX in the β7-β8 loop, although only in 2P-ERK2 (**Fig. 2A-C**, dark green; **Suppl. Fig. S2**, **S4**). Such patterns reflect steric protection from solvent due to the occupancy of ligand in the nucleotide binding site. In contrast, the effects of inhibitors differed in the DFG motif and adjacent β9 strand, where binding of BVD523 and VTX11e led to greater HDX protection compared to GDC0994 (**Fig. 2A-C**, blue; **Fig. 2D**; **Suppl. Fig. S5**). BVD523 and VTX11e also induced HDX protection greater than GDC0994 in regions further from the active site, including the P+1 segment and helix αF (**Fig.**

2A-C, blue; **Fig. 2E,F**). These effects at P+1 and helix αF reveal an allosteric coupling between the active site and distal regions surrounding the activation loop. Thus, solution measurements reported conformation selection for the R-state by BVD523 and VTX11e, but not GDC0994. The similarities in chemical structure between BVD523 and VTX11e suggested that features in their central scaffold and/or right-side regions might contribute to their shared properties of R-state selection.

Conformation selection among small molecule inhibitors of ERK1/2.

To expand the structural diversity of studied compounds, we surveyed a panel of 17 small molecule inhibitors of ERK2 (**Fig. 3A**) that had been produced in the course of chemical development of GDC0994 (Blake et al., 2016). All of these were ATP-competitive, and all inhibited ERK1/2 with subnanomolar Ki. The compounds were chosen for variations in their left-side region, which interacts with the kinase hinge and solvent channel; their central scaffold, which contacts hydrophobic residues from strands β7- β8 and the Gly loop; and their right-side region, which interacts with the Gly loop. The left-side varied between pyrazole and tetrahydropyran groups, the central scaffold alternated pyridone and triazolopyrazine ring structures, and the right-side accommodated many groups with different sizes and chemistries (**Fig. 3B**). Residue contacts with each region are illustrated for VTX11e and GDC0994 in **Fig. 3C**.

HDX-MS was used to examine the effect of each inhibitor on the conformational mobility of ERK2. Thirteen inhibitors (#2, #3, #5-12, #14, #16, #17) produced HDX patterns resembling BVD523 and VTX11e, with strong protection of the DFG motif in both 0P- and 2P-ERK2, and protection of the P+1 segment and helix αF in 2P-ERK2 (**Fig. 4A-C**, **Suppl. Fig. S6A**). In contrast, three inhibitors (#4, #13, #15) showed HDX patterns resembling GDC0994, indicating lesser protection of the DFG motif and no protection in the regions surrounding the activation loop (**Fig. 4A-C**; **Fig. S6B**). One inhibitor (#1) showed strong protection of DFG, but weak protection of the activation loop regions compared to BVD523/VTX11e. The effect of each inhibitor on deuterium uptake was quantified for these peptide segments by summing the differences in centroid mass between apo- and ligand bound enzymes over all time points. This yielded a difference area measurement (dAUC), which was then ranked for each segment. **Fig. 5** shows rankings plotted to compare the DFG and P+1 peptides. The results showed good agreement between the behavior of each segment, with obvious separation in both dimensions between 13 inhibitors clustering with BVD523 and VTX11e, 3 clustering with GDC0994, and one in-between.

The HDX-MS results indicated that many compounds that are structurally distinct from BVD523 and VTX11e nevertheless share properties of R-state selection when bound to 2P-ERK2, while others resemble GDC0994 in maintaining conformational exchange. This was confirmed for a subset of inhibitors by 2D-HMQC NMR, examining methyl probes reporting R⇌L exchange in 2P-ERK2. Seven inhibitors were chosen to represent variations in left-side, central scaffold and right-side substituents. The results showed that four inhibitors that clustered with BVD523 and VTX11e by HDX also shifted populations to 100% R by NMR, while two inhibitors that clustered with GDC0994 maintained R:L population ratios of approximately 80:20 (**Fig. 6A-C**). Inhibitor #1, which appeared between the two main clusters in **Fig. 5**, shifted to the R-state, but only to a partial degree that still allowed exchange (**Fig. 6A-C**). Thus, the HDX and NMR solution measurements are in good agreement and revealed R-state selection in 2P-ERK2 among a majority of the 17 compounds surveyed, even though they are chemically distinct from VTX11e and BVD523.

NMR chemical shifts report inhibitor chemistry and long distance allostery.

Next, we examined NMR chemical shifts to identify [methyl-^{1}H,^{13}C]-ILV probes responsive to binding the different inhibitors (**Suppl. Fig. S7**, **Suppl. Dataset S2**), as distinct from the methyl probes above reporting R⇌L exchange. Chemical shift perturbations from apoenzyme were examined for correlations with different inhibitor features (**Fig. 7**). All inhibitor complexes led to peak disappearances attributed to broadening (indicated by red asterisks below the x-axes in **Suppl. Fig. S7**). These occurred at residues expected to be in direct contact with ligand, based on kinase-inhibitor structures (Roskoski, 2016). They mapped to the Gly loop (V37) and strand β7 (L154) above and below the inhibitor binding site, and the αC-β4 loop (I82) which contacts inhibitor from the back pocket (**Fig. 7,** black; see **Fig. 3C**). Second-shell residues in helix αE (I163), strands β5 (I101) and the N-terminal end (V12) are proximal to residues involved in direct ligand binding, and also appeared broadened.

Four methyl probes showed chemical shifts that could be correlated with the identify of the left-side substituent, which in ERK2:GDC0994 and ERK2:VTX11e are located near the hinge and interact with the solvent-exposed front pocket (**Fig. 3C**; Pegram et al., 2019; Chaikuad et al., 2014; Blake et al., 2016). **Fig. 7** shows the locations of these residue probes in green. Here, chemical shift perturbations separated the inhibitors #4, #6, #8 and #15, which share tetrahydropyran at the left-side position, from #1, #5, #16 and GDC0994, which share pyrazole. Three methyl probes (L105, L155, L161) were located near residues that directly contact the inhibitor left-side, and one (L26) was located in strand β1, nearby hydrophobic side chain (I29)

that contact the pyrazole ring in ERK2:GDC0994 (Pegram et al., 2019; Blake et al., 2016). Thus, several peaks displaying chemical shifts or broadening reported perturbations that were consistent with direct binding interactions.

In contrast, two probes showed chemical shift behaviors that correlated with R-state conformation selection (**Fig. 7**, red). These residues were located away from the active site, within the P+1 segment (I196) and the C-terminal helix αL16 (I345). Here, R-state selective inhibitors (VTX11e, BVD523, #5, #6, #8, #16) induced greater chemical shift perturbations, while inhibitors that retained conformational exchange (GDC0994, #4, #15) were closer to apoenzyme. The location of I196 was consistent with the HDX patterns, showing greater protection in the P+1 loop by each of the R-state selective inhibitors. The location of I345 in helix αL16 suggested an association of the R-state with N-lobe perturbations proximal to helix αC, which interacts with αL16 (**Suppl. Fig. S1**). Thus, NMR identified changes occurring remotely from the ligand binding site that were sensitive to shifts towards the R-state, as reported by HDX-MS (**Figs. 5** and **6**). The results helped confirm that the binding of the new R-state inhibitors is coupled to distal regions, including those around the activation loop.

R-state selection properties correlate with conformational shifts in the N-lobe.

We asked if structural features accompanying R-state selection might be observable by X-ray crystallography. Structures of 2P-ERK2 complexed with inhibitors #8 and #16 were solved (**Suppl. Table S1**, **Dataset S3**, and **Dataset S4**) and compared to previous structures of 2P-ERK2 complexed with VTX11e and GDC0994 (Pegram et al., 2019). Both inhibitors #8 and #16 formed contacts with active site residues that matched those contacting VTX11e and GDC0994 (**Fig. 8A**). They included hydrogen bonds between the left-side aminopyrimidine and the hinge backbone (M106) and tetrahydropyran with the front pocket (K112); direct or water-mediated hydrogen bonds between the central triazolopyridine scaffold and the gatekeeper (Q103), Lys-Glu salt bridge (K52) and DFG motif (D165 backbone amide); and van der Waals interactions between the right-side chlorophenyl or isopentane groups and the Gly loop.

While conformational differences between each of the inhibitor complexes were small, systematic shifts nevertheless appeared in the N-lobe, involving the Gly loop, helix αC and helix αL16. In the co-crystal structure with VTX11e, these elements shifted outwards (away from the ligand and towards the activation loop) relative to GDC0994 (**Fig. 8B**). This difference could be attributed to a residue contact unique to VTX11e, whose right-side 3-chlorobenzyl substituent forms a Cl-π

contact with Y34 on the Gly loop (**Fig. 8B** left panel, see **Fig. 3C**). Y34 in turn forms π-π ring stacking interactions with Y62 on helix αC, suggesting cooperativity effects through ternary anion-π-π interactions (Lucas et al., 2016). These contacts, together with the K52-E69 salt bridge, likely couple movements of the β1- β2- β3 sheet to helix αC, which in turn promotes movement of the adjoining helix αL16. This results in repositioning of helix αC and αL16 to accommodate the bulky chlorobenzyl group on VTX11e and moves the Gly loop to a more closed conformation. In contrast, the corresponding 3-fluoro 4-chlorobenzyl substituent on GDC0994 is positioned higher in the binding site and tilted upwards into the Gly loop relative to VTX11e (**Fig. 8B**, right panel). This holds the Gly loop in a more open conformation and shifts the position of helix αC and αL16 inwards (towards the ligand). Thus, the variations between right-side substituents and their interactions with the Y34-Y62 stack underlies small conformational shifts in the N-lobe that affect domain opening and closure.

Like VTX11e, complexes of 2P-ERK2 with inhibitors #8 and #16 showed outward shifts of the Y34-Y62 stack, the Gly loop, and helices αC and αL16, relative to GDC0994 (**Fig. 8C,D**, left panel). Unlike VTX11e, the 2-chloropyridine and isopentane substituents on inhibitor #8 and #16 respectively were located more than 6 Å from Y34. Both contacted the backbone of strand β1 at angles that allowed but were unlikely to force Gly loop closure (**Fig. 8C,D**, right panels). Inspection of their triazolopyridine central scaffold showed interactions that were distinct from the pyridone scaffold in GDC0994. In GDC0994, the pyridone carbonyl oxygen formed hydrogen bonds with both K52 and a bound water (W1) coordinated to the gatekeeper side chain (Q103) and the DFG main chain amide (D165) (**Fig. 8E**). By contrast, the two nitrogens in the triazole ring of inhibitors #8 and #16 formed separate hydrogen bonds to K52 and W1, respectively. This separation had the effect of shifting the K52-E69 salt bridge position relative to GDC0994. As a result, the Gly loop shifts to a more closed state, allowing the pocket below the Gly loop to accommodate two water molecules that form OH-π interactions with Y34, and favoring outward movement of helices αC and αL16 (**Fig. 8C,D**). In this way, the R-state inhibitors VTX11e, #8 and #16 share small but systematic movements that lead to Gly loop closure and movements of helix αC and αL16 in the direction of the activation loop. Differences were also seen in the hydrogen bond network around the conserved DFG region. Here, a second bound water (W2) formed a bridge between the catalytic residues K52 and D165 in complexes with VTX11e, #8 and #10, but was absent in GDC0994 (**Fig. 8B-D**). This revealed a relayed network of hydrogen bond interactions linking the DFG motif to the K52-E69 salt bridge that appeared common to the three R-state

inhibitors. Conceivably, this might reflect new bonding interactions that favor greater compactness of the active site.

Taken together, the crystal structures showed only small conformational variations among these closely related ATP-competitive inhibitors. Nevertheless, certain features were common to each of the R-state inhibitors, involving Gly loop closure and outward movements of helix αC and αL16. These appeared to be favored either by differential contacts between inhibitor and Y34, or different hydrogen bond configurations between the central scaffold and K52. In each case, coupling to helix αC was enabled by Y34-Y62 and K52-E69 residue interactions. In contrast, the bulky right-side substituent on GDC0994 that prevented Gly loop closure and movements of helix αC/αL16 correlated with retention of conformational exchange.

The results so far revealed correspondence in R-state selection between the amido-linked pyrrole scaffold of VTX11e and BVD523 and the triazolopyridine scaffold of the new inhibitors. We asked what might happen, if the central scaffold were chosen to more closely resemble VTX11e, while choosing a right-side substituent similar to GDC0994. Tizakertib/ATG017/AZD0364 is an ATP competitive ERK inhibitor with a tetrahydropyrrolodiazepenone core that resembles the amidopyrrole group in VTX11e and BVD523, and a right-side 3,4-fluorobenzyl group that resembles the 3-fluoro 4-chlorobenzyl group in GDC0994 (**Fig. 9A**) (Flemington et al., 2020; Ward et al., 2019). Interestingly, the X-ray structure of ATG017 complexed with 0P-ERK2 (**Fig. 9B**, green; PDBID:6SLG, Ward et al., 2019) showed an open Gly loop, relative to complexes of BVD523 and VTX11e with 0P-ERK2 (shown for 0P-ERK2:BVD523, **Fig. 9B**, light blue; PDBID:6GDQ). This was due to rotation of the 3,4-fluorobenzyl ring in ATG017 away from Y34 to form closer interactions with backbone atoms in the β1 and β2 strands. Unlike inhibitors #8 and #16, bound waters between the 3,4-fluorobenzyl ring and Y34 were absent, due to the open Gly loop conformation. As a result, Y34 shifts inwards along with helices αC and αL16, and the side chain of Y64 appears disordered (**Fig. 9B**). The inward direction of this conformational shift suggested that ATG017 might share exchange properties with GDC0994 and the other pyridone-based inhibitors, despite their differences in central scaffold chemistry.

To examine this possibility, ATG017 was complexed with 2P-ERK2 and examined by NMR and HDX-MS. The NMR HMQC spectra revealed a small population shift to the R state, but with overall retention of R⇌L exchange properties, similar to apoenzyme (**Fig. 9C**). Likewise, HDX-MS showed little protection around the P+1 and helix αF segments (**Fig. 9D**), with a pattern that

was clearly distinct from the larger HDX protection induced by VTX11e or BVD523 (**Fig. 2E,F**). Thus, ATG017 showed properties of conformational exchange and inward shifts of helices αC and αL16 that were shared with GDC0994 and inhibitors #4 and #15. This could be attributed to its right-side difluorobenzyl substituent that held the Gly loop in an open state. Interestingly, a bound water (W2) bridging K52 and D165 was present in the ATG017 complex (**Fig. 9B**), and stronger HDX protection around the DFG segment and β9 strand was observed (**Fig. 9D**, **Suppl Fig. S8**). This implies that the HDX protection pattern around the DFG motif is functionally linked to the water bridge (W2) linking K52 and D165. The results show that while changes around the DFG region may contribute to R-state selection, the movements of the Gly loop and helices αC and αL16 appear more essential for conformation selection and allosteric communication.

DISCUSSION

ERK inhibitors are promising therapeutic targets for cancers harboring oncogenic BRAF or RAS with acquired resistance to RAF and MEK inhibitors (Ryan et al., 2015; Morris et al., 2013; Hatzivassiliou et al., 2012; Roskoski et al., 2019; Pan et al., 2022). A feature of ERK2 activation that is somewhat unique among protein kinases is its global exchange behavior, involving millisecond interconversion between at least two states. In this study we present new ATP-competitive inhibitors of ERK1/2 that, despite their chemical divergence from VTX11e and BVD523, nevertheless share properties of R-state selection. They display sensitivity to the conformational differences between the R and L states and the ability to induce long-distance perturbations at the P+1 segment and helix αL16. Crystallographic structures show correlations between the property of R-state selection and small but systematic shifts in the N-lobe that move helices αC and αL16 in the direction of the activation loop. This appears to be facilitated by movements of strands β1-β2-β3 coupled to helix αC. The findings reveal the importance of the positioning of the K52-E69 salt bridge in ERK2, as well as the unique π–π stacking between Tyr residues in the Gly loop and helix αC, in guiding conformation selection for the R-state.

Unlike many other kinases, this regulation of ERK involves relatively small changes in conformation. In 0P-ERK2, the N and C lobes are held apart by the backbone atoms of G167 in the DFG motif, which interdigitates with R65 and Q64 in helix αC (Zhang et al., 1994). This domain separation has been proposed to account for the low activity of unphosphorylated ERK2. Following phosphorylation, residue R65 rotates along with helix αC in the direction of the activation loop and pT183, partially relieving the barrier formed by G167. The resulting domain rotation between N- and C-lobes is only 5 degrees, but it brings K52 closer to D165 by 1.5 Å. Such conformational shifts are smaller than seen in other kinases, but enough to enhance enzymatic activity. The small magnitude of these changes are in part due to structural constraints unique to ERK2. Here, residues in the C-terminal L16 segment extending from the C-lobe to the N-lobe (e.g., Y316, D319, E320 and F327) form close contacts with residues in helices αC and αE and the activation loop (**Suppl. Fig. S9A**). They culminate in helix αL16, where residues I345 and F346 fill a hydrophobic pocket formed by residues in helix αC and the β4-β5 loop (**Suppl. Fig. S9B**). This placement of helix αL16 aligns structurally with hydrophobic motif (HM) sequences at the C-termini of PKA and members of the AGC kinase subfamily (Taylor et al., 2021; Kannan et al, 2007; Baffi and Newton, 2021), as well as cyclins complexed with CDK

(Tatum and Endicott, 2020). Thus helix αL16 coincides with regions in other kinases also involved in long distance allostery.

Many of the key [methyl-^{1}H,^{13}C]-ILV probes that report global exchange behavior in ERK2 are part of the extensive network of hydrophobic residues connecting these substructures. Thus, the side chain of I345 fills a deep hydrophobic pocket formed by T66, L67 and I70 in helix αC, F57 in the β3-αC loop, V99 in strand β5, and M96 in loop β4-β5 (**Suppl. Fig. S9B**). This network also includes contacts formed by αL16 residue F346 with R89, I93 and M96 in the β4-β5 loop, and F352 with L74, I84 and I87 in αC and β4. Furthermore, side chains from F327 and M331 in L16 fill a hydrophobic pocket formed by I72, R75, and F76 in helix αC, V143 in the αE-β6 loop, and V171 in the activation loop (**Suppl. Fig. S9A**). In turn, I72 and F76 form hydrophobic contacts with L73 in helix αC, I138 in helix αE, and F166 in the DFG motif. Thus, αL16 and L16 contact the N-lobe *via* a hydrophobic network that merges with the R-spine (L73, I84, F166). Such extensive packing interactions may help to constrain ERK2, preventing the backbone rotational movements needed to allow a DFG-out configuration (Vijayan et al., 2015), which is never observed in the wild-type kinase. Conceivably, the conformations involved in R⇌L global exchange could reflect systematic movements within this network, which propagate to produce the chemical shift perturbations observed in I345. Although such conformational shifts are small, the coupling between movements of the Gly loop and helices αC and αL16 are complementary to the N-lobe movements seen upon ERK2 phosphorylation. It is remarkable that inhibitors that share similar binding interactions and active site contacts are sensitive to such small conformational differences.

This study shows how HDX-MS and NMR are sensitive to slight perturbations within the active site that lead to significant long-distance responses at the activation loop and P+1 segment. Large structural rearrangements around the activation loop were not obvious in the X-ray structures of 2P-ERK2 complexed with GDC0994, VTX11e, or inhibitors #8 and #16. However, evidence that these measurements truly report conformational changes around pT183 and pY185 was supported by the ability of VTX11e to inhibit their rate of dephosphorylation by MAP kinase phosphatase (MKP3/DUSP6, Pegram et al., 2019). This demonstrates protection of the activation loop by VTX11e binding. Conceivably, the conformation of the activation loop in solution may be more variable than in crystal structures of 2P-ERK2, in part due to lattice restraints. This is suggested by the extensive lattice contacts with the activation loop and P+1 segment in

complexes formed by VTX11e, GDC0994, and inhibitors #8 and #16 (**Suppl. Fig. S10**). In fact, crystal contacts are positioned in a manner that might influence the activation loop in most X-ray structures of ERK2 (Pegram et al., 2023). This highlights the need for solution measurements to more fully understand allosteric regulation in ERK2.

Recently, we conducted extended molecular dynamics simulations (225 μs) starting from the X-ray structure of 2P-ERK2 (PDBID: 2ERK) (Pegram et al., 2023). The results showed unexpected flexibility of the activation loop, which deviated from the X-ray fold in all trajectories and was able to adopt multiple long-lived conformational states with RMSF ≤ 1.2 Å and lasting for more than 5 μs. Each state appeared only after 5 μs, perhaps due to biases introduced by lattice contacts in the starting model. Importantly, the states varied significantly in the contacts formed between the activation loop, L16 and the P+1 segment. These variable activation loop conformations were associated with differential dynamics within the active site, supporting allosteric coupling between these regions. Interestingly, in one of the novel states, the Arg salt bridges formed between pY185 and the P+1 segment were broken, allowing the phosphorylated side chain to move away and form a new salt bridge with helix αC. This reorganization resembled that observed in a co-crystal structure of 2P-ERK2 and the adaptor protein, PEA15 (Mace et al., 2013). The results suggest that distinct conformational states of the activation loop appear thermally accessible and likely to exist in solution. We speculate that they may function to accommodate variable binding modes for substrates and effectors. To the extent this is true, the coupling between the active site and activation loop in ERK2 might allow conformation selective inhibitors to control the binding of regulatory effectors.

Indeed, remote conformational changes induced by conformation selective inhibitors have been shown to alter noncatalytic scaffolding functions of protein kinases *via* interactions with regulatory kinases and phosphatases (Agudo-Ibanez et al., 2023; Leroux and Biondi, 2020; Fang et al., 2020; Sonti et al., 2018; Joseph et al., 2022). Noncatalytic functions of ERK2 include the activation of topoisomerase IIα and poly-ADP ribose polymerase by direct binding of the dual phosphorylated kinase (Shapiro et al., 1999; Cohen-Armon et al., 2006). Preferential binding to 2P-ERK2 has also been shown by a consensus DNA sequence that confers ERK1/2 binding to chromatin DNA and modulates transcription through phosphorylation-independent mechanisms (Hu et al., 2009; Lawrence et al., 2008; McReynolds et al., 2016; Tee et al., 2014). Thus, the ability of R-state inhibitors to control solution conformations of the activation loop may influence emerging noncatalytic functions of ERK.

In summary, the case of ERK2 illustrates how very small conformational changes in protein kinases can lead to considerable effects on activity and inhibition. Correspondingly, small variations between inhibitors which otherwise share similar binding interactions and active site contacts, differentially control long-distance allosteric effects that induce conformational changes at the activation loop. Such differences may be important for cellular responses, by altering the conformation of ERK at a key interface for substate and effector recognition. This highlights the importance of understanding properties of conformation selection in ERK, and how these unique features of ERK regulation impact inhibitor design. The elements of protein architecture that enable small active site movements to yield large effects in distal regions remain an important and exciting feature of MAP kinases to explore in future investigations.

MATERIALS AND METHODS

Reagents and purified proteins. VTX11e, GDC0994 and ATG017 were obtained from Selleck Chemicals (Cat# S7709, S7554, S8708; Houston, TX). Dimethylsulfoxide (DMSO), dithiothreitol (DTT), formic acid and D_2O (99.9%) were obtained from Sigma-Aldrich (Burlington, MA). Ni-NTA agarose was obtained from Qiagen (Germantown, MD). Inhibitors #1-#17 were synthesized in-house, following methods described in WIPO Patents WO2015103137 A1 20150709 and WO2013130976 A1 20130906.

NMR spectroscopy. [*methyl*-^{1}H,^{13}C]-Ile, Leu, and Val-labeled 2P-ERK2 was prepared as described (Xiao et al., 2014, 2015) in buffer containing 50 mM Tris-d11 pH 7.4 (D_2O), 150 mM NaCl, 5 mM $MgSO_4$, 0.1 mM EDTA, 1 mM D,L-1,4-DTT-d10, 100%(v/v) D_2O, and 2.5% (v/v) glycerol-d8. Stock solutions (25 mM) of all inhibitors (VTX11e, BVD523, GDC0994, ATG017, Inhibitors #1, #4, #5, #6, #8, #15, #16) were prepared in DMSO-d6, and added to 2P-ERK2 (150 μM) to form complexes with 100% binding stoichiometry ([inh]: [protein] = 1.2:1). The DMSO-d6 concentration in the final protein sample was ~1% (v/v).

Two-dimensional (2D) ^{1}H-^{13}C heteronuclear multiple quantum coherence (HMQC) spectra of 0P- and 2P-ERK2 were collected on a Varian 900 MHz NMR spectrometer. Data were collected at 25°C and 5°C each for a total time of 10 h. Each spectrum was acquired with nonuniform sampling (NUS) with 160 complex points (900 MHz) in the t_1 (^{13}C) dimension, corresponding to 29.1 ms at 900 MHz, and 1024 complex points in the acquisition period. WURST40 ^{13}C decoupling was applied during the 85 ms acquisition period, and a 1.5 s delay period was used between each scan. The spectral processing was performed with the software package NMRPipe (Delagio et al., 1995). Time domain data in the ^{1}H dimension were apodized by a cosine window function and zero-filled prior to Fourier transformation. The indirect dimension (^{13}C) was apodized by a cosine window function and zero-filled prior to Fourier transformation. NUS spectral reconstruction utilized the SMILE plugin (Ying et al., 2017). Spectral visualization and analysis were achieved using CCPNMR Analysis software (Vranken et al., 2005).

X-ray crystallography. X-ray structure images were created with Pymol 2.3.4 software (Schrödinger LLC, New York, NY). Co-crystals of His_6-human 2P-ERK2 in complex with Inhibitors #8 and #16 were grown at 20°C from sitting drops in 96 wells, mixing 0.5 µL protein + 0.5 µL well solution (20% (w/v) PEG3350, 100 mM Na cacodylate pH 7.2, 600 mM NaCl, 10 mM $MnCl_2$). Crystals were cryoprotected in well solution + 20%(v/v) ethylene glycol prior to data collection. X-

ray diffraction data were collected at Advanced Light Source beamline 5.0.1 and processed using the HKL2000 package (Otwinowski and Minor, 1997). The structure was solved by molecular replacement using the program Phaser with PDBID:2ERK as starting model, and refined using the program REFMAC5 with visual inspection in Coot (CCP4 suite) (Winn et al., 2011).

Kinase inhibition assays. Kinetic parameters (K_i) were determined from aggregate kinase assays of human His_6-ERK2 performed with the fluorescent Omnia peptide substrate, S/T17 (Cat. KNZ1171C, Invitrogen, Carlsbad, CA). Omnia assays contained 50 mM HEPES, pH 7.3, 10 mM $MgCl_2$, 1 mM dithiotheitol, 0.005% Triton-X100, 5 nM ERK2, 6.25 μM S/T17 peptide substrate and 25 μM ATP (corresponding to the observed K_m) in a total reaction volume of 25 μL. Assays were run at ambient temperature in 384-well plates, collecting time points every 50 s for 30 min on an Envision plate reader (PerkinElmer, Waltham, MA) with excitation 340 nm and emission 495 nm. Phosphorylation rates were normalized to controls (no inhibitor),and plotted against inhibitor concentration to obtain IC_{50} values using a four-parameter fit.

Hydrogen-deuterium exchange mass spectrometry (HDX-MS). Wild-type rat 0P-ERK2 and 2P-ERK2 were prepared as described, after bacterial expression from a pET32 plasmid constructed by Marcelo Sousa and Sandra Metzner, U. Colorado, Boulder (Pegram et al. 2019). ERK2 protein (17 μM) was incubated with 20 μM inhibitor (VTX11e, BVD523, GDC0994, ATG017, Inhibitors #1-#17) for 30 min in HDX buffer (50 mM potassium phosphate pH 7.2, 100 mM NaCl, 5 mM DTT, 10 mM $MgCl_2$ and 0.5% (v/v) DMSO from concentrated ligand solutions). Deuterium uptake was initiated by adding 54 μL D_2O (containing an equal concentration of ligand, DMSO, and $MgCl_2$) to 6 μL ERK2 (complexed with or without ligand), to reach a final buffer concentration of 5 mM potassium phosphate pH 7.2, 10 mM NaCl, 0.5 mM DTT, 10 mM $MgCl_2$, and 0.5% DMSO. Reactions were incubated at 25.0°C for varying times between 30 s and 180 min (0.5, 1, 3, 8, 16, 30, 60, 90, 180 min). Exchange was quenched with 48 μL 100 mM potassium phosphate pH 2.2. Additionally, an in-exchange control was performed by addition of quenching solution prior to initiating deuterium uptake, with no incubation period. All reactions were immediately injected in 100 μL volumes onto a Waters nanoAcquity HDX Manager UPLC system for proteolysis on an immobilized pepsin column (Enzymate, Waters, Milford, MA) at 10°C. Proteolysis, as well as peptide desalting (Vanguard Acquity UPLC BEH C18), were carried out in isocratic Solvent A (0.1%(v/v) formic acid in H_2O) with flowrate 100 μL/min. Peptide separations (Waters Acquity UPLC BEH C18, 1.7 μm, 1.0x100 mm) were carried out at 3°C using a 12 min linear gradient from 8-85% Solvent B (0.1% formic acid in acetonitrile) at 40 μL/min.

Peptides were analyzed by ESI-MS/MS using a Waters Synapt G2 HDMS Q-TOF mass spectrometer in positive ion mode. Continuum data were collected over 50-2000 m/z with 0.23 s scan time. Lock mass correction was achieved using Glu-Fibrinogen peptide (MH_2^{+2} = 785.8426 m/z), with resolution = 20,000 at m/z 956. Undeuterated pepsin-cleaved peptides from 0P- or 2P-ERK2 were identified by MS^e sequencing using PLGS 3.0 (Waters). Searches of rat ERK2 allowed nonspecific digestion and variable modifications of oxidized Met and phosphorylated Ser/Thr/Tyr, with parameter settings of intensity threshold = 750 counts, lock mass window = 0.4 Da, and low energy threshold = 135 counts. Peptides were accepted after filtering for high confidence, which required maximum MH^+ error 15 ppm, minimum sequence length 3, maximum sequence length 25, minimum product ions 3, and identification in at least 2 of 4 replicate runs. Deuterium uptake was calculated for high confidence peptides in each hydrogen exchange dataset using DynamX 3.0 (Waters). Raw files were processed using a 0.35 Da lock mass window and a low energy threshold of 100. For every experiment, automated ion assignments for deuterated peptides were manually inspected and validated. The weighted average mass of isotope distributions was calculated for each verified peptide using DynamX, and referenced to the weighted average mass of its unlabeled form. The recorded uptake from the in-exchange control was subtracted from the uptake values of all timepoints (0.5, 1, 3, 8, 16, 30, 60, 90, 180 min) to yield corrected uptake measurements that were used in plots of time courses and dAUC calculations. **Suppl. Dataset S1** contains deuterium uptake values without this correction.

ACKNOWLEDGEMENTS

We are indebted to Drs. Marcelo Sousa, Elan Eisenmesser, and Johannes Rudolph for guidance on structural analyses and many valuable discussions, and to Josh Anderson for insightful discussions about data analysis and presentation. We also thank Drs. Thomas Lee, Chris Ebmeier and Rachel Mehaffey for mass spectrometric analyses of purified proteins, Chang Liu for preliminary HDX studies, and Daniel Lee for Python script coding for HDX datasets. This work was supported by NIH Research Awards R35GM136392 and R01GM114594 (NGA), NIH Instrumentation Awards S10RR026641 and S10OD025267 (mass spectrometry) and S10OD025020 (NMR), and Cancer Center Support Grant P30CA046934 (CU Anschutz NMR Shared Resource Facility).

REFERENCES

Agudo-Ibáñez L, Morante M, García-Gutiérrez L, Quintanilla A, Rodríguez J, Muñoz A, León J, Crespo P. 2023. ERK2 stimulates *MYC* transcription by anchoring CDK9 to the *MYC* promoter in a kinase activity-independent manner. *Science Signaling,* **16**:eadg4193. doi: 10.1126/scisignal.adg4193, PMID: 37463244.

Amatya N, Lin DY, Andreotti AH. 2019. Dynamic regulatory features of the protein tyrosine kinases. *Biochemical Society Transactions* **47**:1101. doi: 10.1042/BST20180590, PMID: 31395755.

Baffi TR, Newton AC. 2022. mTOR regulation of AGC kinases: New twist to an old tail. *Molecular Pharmacology* **101**:213. doi: 10.1124/molpharm.121.000310, PMID: 34155089.

Blake JF, Burkard M, Chan J, Chen H, Chou KJ, Diaz D, Dudley DA, Gaudino JJ, Gould SE, Grina J, Hunsaker T, Liu L, Martinson M, Moreno D, Mueller L, Orr C, Pacheco P, Qin A, Rasor K, Ren L, Robarge K, Shahidi-Latham S, Stults J, Sullivan F, Wang W, Yin J, Zhou A, Belvin M, Merchant M, Moffat J, Schwarz JB. 2016. Discovery of (S)-1-(1-(4-Chloro-3-fluorophenyl)-2-hydroxyethyl)-4-(2-((1-methyl-1H-pyrazol-5-yl)amino)pyrimidin-4-yl)pyridin-2(1H)-one (GDC-0994), an extracellular signal-regulated kinase 1/2 (ERK1/2) inhibitor in early clinical development. *Journal of Medicinal Chemistry* **59**:5650. doi: 10.1021/acs.jmedchem.6b00389, PMID: 27227380.

Canagarajah BJ, Khokhlatchev A, Cobb MH, Goldsmith EJ. 1997. Activation mechanism of the MAP kinase ERK2 by dual phosphorylation. *Cell* **90**:859. doi: 10.1016/s0092-8674(00)80351-7, PMID: 9298898.

Canon J, Rex K, Saiki AY, Mohr C, Cooke K, Bagal D, Gaida K, Holt T, Knutson CG, Koppada N, Lanman BA, Werner J, Rapaport AS, San Miguel T, Ortiz R, Osgood T, Sun JR, Zhu X, McCarter JD, Volak LP, Houk BE, Fakih MG, O'Neil BH, Price TJ, Falchook GS, Desai J, Kuo J, Govindan R, Hong DS, Ouyang W, Henary H, Arvedson T, Cee VJ, Lipford JR. 2019. The clinical KRAS(G12C) inhibitor AMG 510 drives anti-tumour immunity. *Nature* **575**:217. doi: 10.1038/s41586-019-1694-1, PMID: 31666701.

Chaikuad A, Tacconi EM, Zimmer J, Liang Y, Gray NS, Tarsounas M, Knapp S. 2014. A unique inhibitor binding site in ERK1/2 is associated with slow binding kinetics. *Nature Chemical Biology* **10**:853. doi: 10.1038/nchembio.1629, PMID: 25195011.

Chen P, Liu Y, Deng M, Wang J, Hoenemann D, Lynch K, Mei J, Shan B, Hou B. 2021. Synergistic effect of the combination of ATG-017, and ERK1/2 inhibitor, and immune checkpoint inhibitor in preclinical cancer models. *Journal for Immunotherapy of Cancer* **9**(Suppl 2):A638.

Cohen-Armon M, Visochek L, Rozensal D, Kalal A, Geistrikh I, Klein R, Bendetz-Nezer S, Yao Z, Seger R. 2006. DNA-independent PARP-1 activation by phosphorylated ERK2 increases Elk1 activity: a link to histone acetylation. *Molecular Cell* **25**:297. doi: 10.1016/j.molcel.2006.12.012, PMID: 17244536.

Delaglio F, Grzesiek S, Vuister GW, Zhu G, Pfeifer J, Bax A. 1995. NMRPipe: a multidimensional spectral processing system based on UNIX pipes. *Journal of Biomolecular NMR* 6:277. doi: 10.1007/BF00197809, PMID: 8520220.

Fang L, Vilas-Boas J, Chakraborty S, Potter ZE, Register AC, Seeliger MA, Maly DJ. 2020. How ATP-competitive inhibitors allosterically modulate tyrosine kinases that contain a Src-like regulatory architecture. 2020. *ACS Chemical Biology* **15**:2005. doi: 10.1021/acschembio.0c00429, PMID: 32479050.

Flemington V, Davies EJ, Robinson D, Sandin LC, Delpuech O, Zhang P, Hanson L, Farrington P, Bell S, Falenta K, Gibbons FD, Lindsay N, Smith A, Wilson J, Roberts K, Tonge M, Hopcroft P, Willis SE, Roudier MP, Rooney C, Coker EA, Jaaks P, Garnett MJ, Fawell SE, Jones CD, Ward RA, Simpson I, Cosulich SC, Pease JE, Smith PD. 2021. AZD0364 is a potent and selective ERK1/2 inhibitor that enhances antitumor activity in *KRAS*-mutant tumor models when combined with the MEK inhibitor, selumetinib. *Molecular Cancer Therapeutics* **20**:238. doi: 10.1158/1535-7163.MCT-20-0002, PMID: 33273059.

Germann UA, Furey BF, Markland W, Hoover RR, Aronov AM, Roix JJ, Hale M, Boucher DM, Sorrell DA, Martinez-Botella G, Fitzgibbon M, Shapiro P, Wick MJ, Samadani R, Meshaw K, Groover A, DeCrescenzo G, Namchuk M, Emery CM, Saha S, Welsch DJ. 2017. Targeting the MAPK signaling pathway in cancer: Promising preclinical activity with the novel selective ERK1/2 inhibitor BVD-523 (Ulixertinib). *Molecular Cancer Therapeutics* **16**:2351. doi: 10.1158/1535-7163.MCT-17-0456, PMID: 28939558.

Goodwin CM, Waters AM, Klomp JE, Javaid S, Bryant KL, Stalnecker CA, Drizyte-Miller K, Papke B, Yang R, Amparo AM, Ozkan-Dagliyan I, Baldelli E, Calvert V, Pierobon M, Sorrentino JA, Beelen AP, Bublitz N, Lüthen M, Wood KC, Petricoin EF, Sers C, McRee AJ, Cox AD, Der CJ. 2023. Combination therapies with CDK4/6 inhibitors to treat KRAS-mutant pancreatic cancer. *Cancer Research* **83**:141. doi: 10.1158/0008-5472.CAN-22-0391, PMID: 36346366.

Grierson PM, Tan B, Pedersen KS, Park H, Suresh R, Amin MA, Trikalinos NA, Knoerzer D, Kreider B, Reddy A, Liu J, Der CJ, Wang-Gillam A, Lim KH. 2023. Phase Ib study of ulixertinib plus gemcitabine and nab-paclitaxel in patients with metastatic pancreatic adenocarcinoma. *Oncologist* **28**:e115. doi: 10.1093/oncolo/oyac237, PMID: 36427020.

Halle BR, Johnson DB. 2021. Defining and targeting BRAF mutations in solid tumors. *Current Treatment Options in Oncology* **22**:30. doi: 10.1007/s11864-021-00827-2, PMID: 33641072.

Hatzivassiliou G, Liu B, O'Brien C, Spoerke JM, Hoeflich KP, Haverty PM, Soriano R, Forrest WF, Heldens S, Chen H, Toy K, Ha C, Zhou W, Song K, Friedman LS, Amler LC, Hampton GM, Moffat J, Belvin M, Lackner MR. 2012. ERK inhibition overcomes acquired resistance to MEK inhibitors. *Molecular Cancer Therapeutics* **11**:1143. doi: 10.1158/1535-7163.MCT-11-1010, PMID: 22402123.

Heightman TD, Berdini V, Braithwaite H, Buck IM, Cassidy M, Castro J, Courtin A, Day JEH, East C, Fazal L, Graham B, Griffiths-Jones CM, Lyons JF, Martins V, Muench S, Munck JM, Norton D, O'Reilly M, Palmer N, Pathuri P, Reader M, Rees DC, Rich SJ, Richardson C, Saini H, Thompson NT, Wallis NG, Walton H, Wilsher NE, Woolford AJ, Cooke M, Cousin D, Onions S, Shannon J, Watts J, Murray CW. 2018. Fragment-based discovery of a potent, orally bioavailable inhibitor that modulates the phosphorylation and catalytic activity of ERK1/2. *Journal of Medicinal Chemistry* **61**:4978. doi: 10.1021/acs.jmedchem.8b00421. PMID: 29775310.

Hu S, Xie Z, Onishi A, Yu X, Jiang L, Lin J, Rho HS, Woodard C, Wang H, Jeong JS, Long S, He X, Wade H, Blackshaw S, Qian J, Zhu H. 2009. Profiling the human protein-DNA interactome

reveals ERK2 as a transcriptional repressor of interferon signaling. *Cell* **139**:610. doi: 10.1016/j.cell.2009.08.037, PMID: 19879846.

Iverson DB, Xiao Y, Jones DN, Eisenmesser EZ, Ahn NG. 2020. Activation loop dynamics are coupled to core motions in extracellular signal-regulated kinase-2. *Biochemistry* **59**:2698. doi: 10.1021/acs.biochem.0c00485, PMID: 32643366.

Joseph RE, Lowe J, Fulton DB, Engen JR, Wales TE, Andreotti AH. 2022. The conformational state of the BTK substrate PLCγ contributes to ibrutinib resistance. *Journal of Molecular Biology* **434**:167422. doi: 10.1016/j.jmb.2021.167422, PMID: 34954235.

Kannan N, Haste N, Taylor SS, Neuwald AF. 2007. The hallmark of AGC kinase functional divergence is its C-terminal tail, a cis-acting regulatory module. *Proceedings of the National Academy of Science USA* **104**:1272. doi: 10.1073/pnas.0610251104, PMID: 17227859.

Kong Y, Chen P, Jiang L, Jiang B, Mei J, Shan B, Hou B. 2023. Synergistic effects of the combination of ERK1/2 with EGFR, KRASG12C, CDK4/6 and PD-L1 inhibition for cancer treatment. In: Annual Meeting of the American Association of Cancer Research, April 14-19, 2023, Orlando, Florida.

Lavoie H, Gagnon J, Therrien M. 2020. ERK signalling: a master regulator of cell behaviour, life and fate. *Nature Reviews in Molecular Cell Biology* **21**:607. doi: 10.1038/s41580-020-0255-7, PMID: 32576977.

Lawrence MC, McGlynn K, Shao C, Duan L, Naziruddin B, Levy MF, Cobb MH. 2008. Chromatin-bound mitogen-activated protein kinases transmit dynamic signals in transcription complexes in beta-cells. *Proceedings of the National Academy of Science USA*. **105**:13315. doi: 10.1073/pnas.0806465105, PMID: 18755896.

Lechtenberg BC, Mace PD, Sessions EH, Williamson R, Stalder R, Wallez Y, Roth GP, Riedl SJ, Pasquale EB. 2017. Structure-guided strategy for the development of potent bivalent ERK inhibitors. *ACS Medicinal Chemistry Letters* **8**:726. doi: 10.1021/acsmedchemlett.7b00127, PMID: 28740606.

Lee T, Hoofnagle AN, Kabuyama Y, Stroud J, Min X, Goldsmith EJ, Chen L, Resing KA, Ahn NG. 2004. Docking motif interactions in MAP kinases revealed by hydrogen exchange mass spectrometry. *Molecular Cell* **14**:43. doi: 10.1016/s1097-2765(04)00161-3, PMID: 15068802.

Leroux AE, Biondi RM. 2020. Renaissance of allostery to disrupt protein kinase interactions. *Trends in Biochemical Sciences* **45**:27. doi: 10.1016/j.tibs.2019.09.007, PMID: 31690482.
Mace PD, Wallez Y, Egger MF, Dobaczewska MK, Robinson H, Pasquale EB, Riedl SJ. 2013. Structure of ERK2 bound to PEA-15 reveals a mechanism for rapid release of activated MAPK. *Nature Communications* **4**:1681. doi: 10.1038/ncomms2687, PMID: 23575685.

Lucas X, Bauzá A, Frontera A, Quiñonero D. 2016. A thorough anion-π interaction study in biomolecules: On the importance of cooperativity effects. *Chemical Science* **7**:1038-1050. doi: 10.1039/c5sc01386k, PMID: 29899893.

McReynolds AC, Karra AS, Li Y, Lopez ED, Turjanski AG, Dioum E, Lorenz K, Zaganjor E, Stippec S, McGlynn K, Earnest S, Cobb MH. 2016. Phosphorylation or mutation of the ERK2 activation

loop alters oligonucleotide binding. *Biochemistry* **55**:1909. doi: 10.1021/acs.biochem.6b00096, PMID: 26950759.

Morris EJ, Jha S, Restaino CR, Dayananth P, Zhu H, Cooper A, Carr D, Deng Y, Jin W, Black S, Long B, Liu J, Dinunzio E, Windsor W, Zhang R, Zhao S, Angagaw MH, Pinheiro EM, Desai J, Xiao L, Shipps G, Hruza A, Wang J, Kelly J, Paliwal S, Gao X, Babu BS, Zhu L, Daublain P, Zhang L, Lutterbach BA, Pelletier MR, Philippar U, Siliphaivanh P, Witter D, Kirschmeier P, Bishop WR, Hicklin D, Gilliland DG, Jayaraman L, Zawel L, Fawell S, Samatar AA. 2013. Discovery of a novel ERK inhibitor with activity in models of acquired resistance to BRAF and MEK inhibitors. *Cancer Discovery* **3**:742. doi: 10.1158/2159-8290.CD-13-0070, PMID: 23614898.

Otwinowski Z, Minor W. 1997. Processing of X-ray diffraction data collected in oscillation mode. *Methods Enzymology,* **276**:307-326. doi: 10.1016/S0076-6879(97)76066-X, PMID: 27754618.

Pan X, Pei J, Wang A, Shuai W, Feng L, Bu F, Zhu Y, Zhang L, Wang G, Ouyang L. 2022. Development of small molecule extracellular signal-regulated kinases (ERKs) inhibitors for cancer therapy. *Acta Pharmceutica Sinica B* **12**:2171-2192. doi: 10.1016/j.apsb.2021.12.022, PMID: 35646548.

Pegram L, Riccardi D, Ahn N. 2023. Activation loop plasticity and active site coupling in the MAP kinase, ERK2. *bioRxiv* Apr 15:2023.04.15.537040. doi: 10.1101/2023.04.15.537040, PMID: 37090603.

Pegram LM, Liddle JC, Xiao Y, Hoh M, Rudolph J, Iverson DB, Vigers GP, Smith D, Zhang H, Wang W, Moffat JG, Ahn NG. 2019. Activation loop dynamics are controlled by conformation-selective inhibitors of ERK2. *Proceedings of the National Academy of Science USA* **116**:15463. doi: 10.1073/pnas.1906824116, PMID: 31311868.

Plotnikov A, Zehorai E, Procaccia S, Seger R. 2011. The MAPK cascades: signaling components, nuclear roles and mechanisms of nuclear translocation. *Biochimica Biophysica Acta* **1813**:1619. doi: 10.1016/j.bbamcr.2010.12.012, PMID: 21167873.

Roskoski R. 2012. ERK1/2 MAP kinases: structure, function, and regulation. *Pharmacological Research* **66**:105. doi: 10.1016/j.phrs.2012.04.005, PMID: 22569528.

Roskoski R. 2015. Classification of small molecule protein kinase inhibitors based upon the structures of their drug-enzyme complexes. *Pharmacological Research* **103**:26. doi: 10.1016/j.phrs.2015.10.021, PMID: 26529477.

Roskoski R. 2019. Targeting ERK1/2 protein-serine/threonine kinases in human cancers. *Pharmacological Research* **142**:151. doi: 10.1016/j.phrs.2019.01.039, PMID: 30794926.

Rudolph J, Xiao Y, Pardi A, Ahn NG. 2014. Slow inhibition and conformation selective properties of extracellular signal-regulated kinase 1 and 2 inhibitors. *Biochemistry* **54**:22. doi: 10.1021/bi501101v, PMID: 25350931.

Ryan MB, Der CJ, Wang-Gillam A, Cox AD. Targeting *RAS*-mutant cancers: is ERK the key? *Trends in Cancer***1**:183. doi: 10.1016/j.trecan.2015.10.001, PMID: 26858988.

Ryan MB, Fece de la Cruz F, Phat S, Myers DT, Wong E, Shahzade HA, Hong CB, Corcoran RB. 2020. Vertical pathway inhibition overcomes adaptive feedback resistance to KRAS^{G12C} inhibition. *Clinical Cancer Research* **26**:1633. doi: 10.1158/1078-0432, PMID: 31776128.

Sang D, Pinglay S, Wiewiora RP, Selvan ME, Lou HJ, Chodera JD, Turk BE, Gümüş ZH, Holt LJ. 2019. Ancestral reconstruction reveals mechanisms of ERK regulatory evolution. *Elife* **8**:e38805. doi: 10.7554/eLife.38805, PMID: 31407663.

Shapiro PS, Whalen AM, Tolwinski NS, Wilsbacher J, Froelich-Ammon SJ, Garcia M, Osheroff N, Ahn NG. 1999. Extracellular signal-regulated kinase activates topoisomerase II-alpha through a mechanism independent of phosphorylation. *Molecular Cell Biology* **19**:3551. doi: 10.1128/MCB.19.5.3551, PMID: 10207078.

Sigaud R, Rösch L, Gatzweiler C, Benzel J, von Soosten L, Peterziel H, Selt F, Najafi S, Ayhan S, Gerloff XF, Hofmann N, Büdenbender I, Schmitt L, Foerster KI, Burhenne J, Haefeli WE, Korshunov A, Sahm F, van Tilburg CM, Jones DTW, Pfister SM, Knoerzer D, Kreider BL, Sauter M, Pajtler KW, Zuckermann M, Oehme I, Witt O, Milde T. 2023. The first-in-class ERK inhibitor ulixertinib shows promising activity in mitogen-activated protein kinase (MAPK)-driven pediatric low-grade glioma models. *Neuro-Oncology* **25**:566. doi: 10.1093/neuonc/noac183, PMID: 35882450.

Smorodinsky-Atias K, Goshen-Lago T, Goldberg-Carp A, Melamed D, Shir A, Mooshayef N, Beenstock J, Karamansha Y, Darlyuk-Saadon I, Livnah O, Ahn NG, Admon A, Engelberg D. 2016. Intrinsically active variants of Erk oncogenically transform cells and disclose unexpected autophosphorylation capability that is independent of TEY phosphorylation. *Molecular Biology of the Cell* **27**:1026. doi: 10.1091/mbc.E15-07-0521, PMID: 26658610.

Sonti R, Hertel-Hering I, Lamontanara AJ, Hantschel O, Grzesiek S. 2018. ATP site ligands determine the assembly state of the Abelson kinase regulatory core via the activation loop conformation. *Journal of the American Chemical Society* **140**:1863. doi: 10.1021/jacs.7b12430, PMID: 29319304.

Sullivan RJ, Infante JR, Janku F, Wong DJL, Sosman JA, Keedy V, Patel MR, Shapiro GI, Mier JW, Tolcher AW, Wang-Gillam A, Sznol M, Flaherty K, Buchbinder E, Carvajal RD, Varghese AM, Lacouture ME, Ribas A, Patel SP, DeCrescenzo GA, Emery CM, Groover AL, Saha S, Varterasian M, Welsch DJ, Hyman DM, Li BT. 2018. First-in-class ERK1/2 inhibitor ulixertinib (BVD-523) in Patients with MAPK Mutant Advanced Solid Tumors: Results of a Phase I Dose-escalation and expansion study. *Cancer Discovery* **8**:184. doi: 10.1158/2159-8290.CD-17-1119, PMID: 29247021.

Tangella LP, Clark ME, Gray ES. 2021. Resistance mechanisms to targeted therapy in BRAF-mutant melanoma - A mini review. *Biochimica Biophysica Acta* **1865**:129736. doi: 10.1016/j.bbagen.2020.129736, PMID: 32956754.

Tatum NJ, Endicott JA. 2020. Chatterboxes: the structural and functional diversity of cyclins. *Seminars in Cell and Developmental Biology* **107**:4. doi: 10.1016/j.semcdb.2020.04.021, PMID: 32414682.

Taylor SS, Meharena HS, Kornev AP. 2019. Evolution of a dynamic molecular switch. *IUBMB Life* **71**:672. doi: 10.1002/iub.2059, PMID: 31059206.

Taylor SS, Søberg K, Kobori E, Wu J, Pautz S, Herberg FW, Skålhegg BS. 2022. The tails of protein kinase A. *Molecular Pharmacology* **101**:219. doi: 10.1124/molpharm.121.000315, PMID: 34330820.

Tee WW, Shen SS, Oksuz O, Narendra V, Reinberg D. 2014. Erk1/2 activity promotes chromatin features and RNAPII phosphorylation at developmental promoters in mouse ESCs. *Cell* **156**:678. doi: 10.1016/j.cell.2014.01.009, PMID: 24529373.

Varga A, Soria JC, Hollebecque A, LoRusso P, Bendell J, Huang SA, Wagle MC, Okrah K, Liu L, Murray E, Sanabria-Bohorquez SM, Tagen M, Dokainish H, Mueller L, Burris H. 2020. A first-in-human Phase I study to evaluate the ERK1/2 inhibitor GDC-0994 in patients with advanced solid tumors. *Clinical Cancer Research* **26**:1229. doi: 10.1158/1078-0432.CCR-19-2574, PMID: 31848189.

Vijayan RS, He P, Modi V, Duong-Ly KC, Ma H, Peterson JR, Dunbrack RL Jr, Levy RM. 2015. Conformational analysis of the DFG-out kinase motif and biochemical profiling of structurally validated type II inhibitors. *Journal of Medicinal Chemistry* **58**:466. doi: 10.1021/jm501603h, PMID: 25478866.

Vranken WF, Boucher W, Stevens TJ, Fogh RH, Pajon A, Llinas M, Ulrich EL, Markley JL, Ionides J, Laue ED. 2005. The CCPN data model for NMR spectroscopy: development of a software pipeline. *Proteins* 59:687. doi: 10.1002/prot.20449, PMID: 15815974.

Ward RA, Anderton MJ, Bethel P, Breed J, Cook C, Davies EJ, Dobson A, Dong Z, Fairley G, Farrington P, Feron L, Flemington V, Gibbons FD, Graham MA, Greenwood R, Hanson L, Hopcroft P, Howells R, Hudson J, James M, Jones CD, Jones CR, Li Y, Lamont S, Lewis R, Lindsay N, McCabe J, McGuire T, Rawlins P, Roberts K, Sandin L, Simpson I, Swallow S, Tang J, Tomkinson G, Tonge M, Wang Z, Zhai B. 2019. Discovery of a potent and selective oral inhibitor of ERK1/2 (AZD0364) that Is efficacious in both monotherapy and combination therapy in models of nonsmall cell lung cancer (NSCLC). *Journal of Medicinal Chemistry* **62**:11004. doi: 10.1021/acs.jmedchem.9b01295, PMID: 31710489.

Winn MD, Ballard CC, Cowtan KD, Dodson EJ, Emsley P, Evans PR, Keegan RM, Krissinel EB, Leslie AG, McCoy A, McNicholas SJ, Murshudov GN, Pannu NS, Potterton EA, Powell HR, Read RJ, Vagin A, Wilson KS. 2011. Overview of the CCP4 suite and current developments. *Acta Crystallographica D* **67**:2352. doi: 10.1107/S0907444910045749, PMID: 21460441.

Wu J, Liu D, Offin M, Lezcano C, Torrisi JM, Brownstein S, Hyman DM, Gounder MM, Abida W, Drilon A, Harding JJ, Sullivan RJ, Janku F, Welsch D, Varterasian M, Groover A, Li BT, Lacouture ME. 2021. Characterization and management of ERK inhibitor associated dermatologic adverse events: analysis from a nonrandomized trial of ulixertinib for advanced cancers. *Investigational New Drugs* **39**:785. doi: 10.1007/s10637-020-01035-9, PMID: 33389388.

Xiao Y, Lee T, Latham MP, Warner LR, Tanimoto A, Pardi A, Ahn NG. 2014. Phosphorylation releases constraints to domain motion in ERK2. *Proceedings of the National Academy of Science USA* **111**:2506. doi: 10.1073/pnas.1318899111, PMID: 24550275.

Xiao Y, Warner LR, Latham MP, Ahn NG, Pardi A. 2015. Structure-based assignment of Ile, Leu, and Val methyl groups in the active and inactive forms of the mitogen-activated protein kinase extracellular signal-regulated kinase 2. *Biochemistry* **54**:4307. doi: 10.1021/acs.biochem.5b00506, PMID: 26132046.

Ying J, Delaglio F, Torchia DA, Bax A. 2017. Sparse multidimensional iterative lineshape-enhanced (SMILE) reconstruction of both non-uniformly sampled and conventional NMR data. *Journal of Biomolecular NMR*, **68**:101-118. doi: 10.1007/s10858-016-0072-7, PMID: 27866371.

Yu Y, Zhao Y, Choi J, Shi Z, Guo L, Elizarraras J, Gu A, Cheng F, Pei Y, Lu D, Fabbri M, Agarwal S, Zhang C, Jung SY, Foster JH, Yang J. 2022. ERK inhibitor ulixertinib inhibits high-risk neuroblastoma growth in vitro and in vivo. *Cancers (Basel)* **14**(:5534. doi: 10.3390/cancers14225534, PMID: 36428626.

Zhang F, Strand A, Robbins D, Cobb MH, Goldsmith EJ. 1994. Atomic structure of the MAP kinase ERK2 at 2.3 A resolution. *Nature* **367**:704. doi: 10.1038/367704a0, PMID: 8107865.

Zhang J, Shapiro P, Pozharski E. 2012. Structure of extracellular signal-regulated kinase 2 in complex with ATP and ADP. *Acta Crystallographica Section F Structural Biology Communications* **68**:1434. doi: 10.1107/S1744309112042972, PMID: 23192020.

FIGURE LEGENDS

Figure 1. BVD523 and VTX11e stabilize the R-state in 2P-ERK2. (A) Chemical structures of the ATP-competitive ERK1/2 inhibitors, BVD523, VTX11e and GDC0994. **(B-D)** 2D-HMQC spectra collected at 25°C and 5°C, showing [methyl ^{1}H,^{13}C] peaks of residues **(B)** I72, **(C)** L220 and **(D)** L242, which report R and L conformers. Their locations in the ERK2 structure are shown in **Suppl. Fig. S1**. 2P-ERK2 complexed with BVD523 and VTX11e (shown in blue) shift to 100% R at all temperatures, while 2P-ERK2 complexed with GDC0994 (shown in grey) retains conformational exchange between R:L populations of 80:20, similar to the apoenzyme. Previous studies show that 0P-ERK2 complexed with all inhibitors retains the L conformer seen in the apoenzyme (Pegram et al., 2019).

Figure 2. Binding of R-state inhibitors reveals allosteric coupling between the active site and the activation loop. (A-C) Summary of HDX experiments indicating regions that change in deuterium uptake upon binding of **(A)** BVD523, **(B)** VTX11e, and **(C)** GDC0994. (**D-F**) HDX time courses showing effects of inhibitors on deuterium uptake at the **(D)** DFG motif (peptide 161-168: LKICDFGL), **(E)** P+1 segment (peptide 191-198, YRAPEIML), and **(F)** helix αF (peptide 203-210: YTKSIDIW). Colored segments in panels **A-C** indicate regions where HDX decreases or increases upon binding each inhibitor at saturating concentration (20 μM). Full peptide coverage and locations of segments that undergo changes in HDX with inhibitor binding are shown in **Suppl. Figs. S2** and **S3**. Highlighted in light green in panels **A-C** are regions where a similar degree of HDX protection is seen with all inhibitors in both 0P-ERK2 and 2P-ERK2 (Gly loop, hinge, helices αC, αE and αL16). HDX protection is similar with all inhibitors in strands β7-β8 (dark green) in 2P-ERK2, but not 0P-ERK2. Time courses for these peptides are shown in **Suppl. Fig. S4**. Highlighted in light blue are regions where BVD523, VTX11e or GDC0994 lead to decreased HDX uptake around the DFG motif, in 0P-ERK2 or 2P-ERK2. Highlighted in dark blue are regions where BVD523 and VTX11e lead to increased HDX protection, compared to GDC0994. These occur only in 2P-ERK2, and include the DFG motif and adjacent strand β9, as well as the P+1 segment and helix αF. Time courses for strand β9 are shown in **Suppl. Fig. S5**. Full HDX datasets for all inhibitors are presented in **Suppl. Dataset S1**. Crystal structures shown in panels **A-C** are **(A)** PDBID: 6GDQ (left) and 2ERK (right); **(B)** PDBID: 4QTE (left) and 6OPK (right); **(C)** PDBID: 5K4I (left) and 6OPH (right).

Figure 3. Novel ATP-competitive inhibitors of ERK1/2. **(A)** A panel of 17 novel ERK1/2 inhibitors surveyed in this study. K_i measurements were made using kinase assays for phosphorylation of Omnia peptide substrate (Invitrogen). **(B)** Variations among ERK1/2 inhibitors in their left-side, central scaffold, and a sampling of right-side substituents. **(C)** Contacts formed by VTX11e and GDC0994 with active site residues in 2P-ERK2, based on published X-ray structures (PDBID:6OPK, PDBID:6OPH).

Figure 4. HDX assays survey conformation selection among compounds in the ERK inhibitor panel. HDX measurements performed with representative inhibitors shown in **Fig. 3**, chosen for variations in their left-side, central scaffold, and right-side substituents. Time courses show deuterium uptake at the **(A)** DFG motif (peptide 161-168: LKICDFGL), **(B)** P+1 segment (peptide 191-198, YRAPEIML), and helix αF (peptide 203-210: YTKSIDIW). Enhanced HDX protection (strongly decreased uptake) in each segment by inhibitors #5, #6, #8 and #16 (blue) suggest properties of conformation selection for the R-state, while lower protection by inhibitors #4 and #15 (grey) suggest retention of conformational exchange. Inhibitor #1 (cyan) shows HDX properties intermediate to these two groups. HDX time courses for the full set of 17 inhibitors are shown in **Suppl. Fig. S6A,B**.

Figure 5. ERK inhibitors differentially cluster with VTX11e/BVD523 or GDC0994. Effects of inhibitors on HDX were quantified by a difference AUC measurement, which calculates dAUC = $\Sigma_t(HDX_{Apo} - HDX_{Inhibitor})_t$ over all time points. **(A)** Plot comparing dAUC for the DFG motif (peptide 161-168) *vs* P+1 segment (peptide 191-198) reveals 13 inhibitors clustered with VTX11e/BVD523, 3 inhibitors clustered with GDC0994, and one inhibitor with intermediate properties. Labels mark the representative set of inhibitors shown in **Fig. 4**. **(B)** dAUC values for each inhibitor.

Figure 6. 2D-HMQC NMR confirms R-state selection by ERK inhibitors. 2D(^{1}H,^{13}C)-HMQC NMR spectra were collected on 2P-ERK2 at 25°C and 5°C. Effects on [methyl ^{1}H,^{13}C] peaks of residues **(A)** I72, **(B)** L220 and **(C)** L242 are shown for the representative set of inhibitors in **Fig. 4**. Inhibitors #5, #6, #8 and #16 (shown in blue) shifted the R⇌L equilibrium to 100% R at all temperatures, confirming R-state selection as suggested by their HDX behaviors in **Figs. 4** and **5**. Inhibitors #4 and #15 (in grey) retained R:L populations comparable to those with GDC0994. Inhibitor #1 (in cyan) showed partial selection for the R state but retained conformational exchange, as evidenced by an L state population present at 5°C.

Figure 7. NMR chemical shift patterns reveal long distance perturbations by R-state inhibitors. 2D-HMQC NMR spectra of 2P-ERK2 at 25°C showing [methyl $^{1}H,^{13}C$] peaks with significant changes in chemical shift upon binding ERK inhibitors. NMR peaks colored blue correspond to inhibitors characterized as R-state selective (VTX11e, BVD523, #5, #6, #8, #16). Peaks colored grey correspond to inhibitors that allow conformational exchange (GDC0994, #4, #15). Peaks in cyan correspond to inhibitor #1, which shows partial R-state selection. Shown in red spheres on the X-ray structure (PDBID:6OPK) are residues (I196, I345) that separate the R-state selective inhibitors from those that allow exchange. Green spheres are residues (L26, L105, L155, L161) that separate inhibitors with left-side tetrahydropyran (#4, #6, #8, #15) from other substituents. Black spheres are residues (V12, V37, I82, I101, L154, I163) that broaden upon binding all inhibitors; these together with residues in orange (I138, L148) reflect first- and second-sphere regions of contact around the binding site. Chemical shifts and chemical shift perturbations ($\Delta\delta$) for all assigned residues are shown in **Suppl. Fig. S7** and **Suppl. Dataset S2**.

Figure 8. R-state inhibitors promote outward movements of N-lobe structural elements. **(A)** Summary of contacts formed by inhibitors #8 and #16 with active site residues in co-crystal structures with 2P-ERK2. **(B)** The active site of 2P-ERK2 complexed with GDC0994 (PDBID:6OPH, grey) and VTX11e (PDBID:6OPK, blue) (Pegram et al, 2019). *Left panel:* Front view showing movement of the Gly loop, helix αC and helix αL16 in an "outward" direction (away from the inhibitor) upon binding of VTX11e (blue), relative to GDC0994 (grey). The movement can be attributed to the right-side 3-chlorobenzyl substituent in VTX11e which interacts with the π orbital of Y34 in the Gly loop (Cl-π distance, 3.5 Å). In turn, π–π stacking interactions between Y34 and Y62 couples movements of the Gly loop to helix αC. *Right panel:* Side view showing left-side hydrogen bond contacts with main chain atoms of hinge residue M106, as typical of ATP-competitive kinase inhibitors. **(C,D)** Active site of 2P-ERK2 complexed with GDC0994 (grey) and **(C)** inhibitor #8 (slate) or **(D)** inhibitor #16 (cyan). Like VTX11e, inhibitors #8 and #16 move the Gly loop, helix αC and helix αL16 outward, relative to GDC0994. Left panels **B-D** show that all inhibitor complexes share a bound water (W1) bridging the central scaffold to the gatekeeper residue in ERK2 (Q103). Right panels show that a bound water (W2) bridges active site residues K52 and D165 in complexes with VTX11e, inhibitor #8 and inhibitor #16, but not GDC0994. **(E)** Overlay of GDC0994 (grey), inhibitor #8 (slate) and inhibitor #16 (cyan). The relative N-lobe movements in panels **C** and **D** may be explained by differential hydrogen bonding of K52 and W1 to the triazolopyridine central scaffold of inhibitors #8 and #16, distinct from the pyridone scaffold

of GDC0994. The position of the hydrogen bond of the triazole nitrogen with K52 relative to the pyridone oxygen moves the K52-E69 salt bridge in an outward direction in inhibitors #8 and #10 relative to GDC0994. Structures were superpositioned by aligning Cα atoms within the C-terminal domain (residues 109-141, 205-245, 272-310).

Figure 9. ATG017 promotes Gly loop opening and inward movement of N-lobe elements. **(A)** Summary of contacts formed by inhibitor ATG017 with active site residues in a co-crystal structure with 0P-ERK2 (Ward et al., 2019). **(B)** The active site of 0P-ERK2 complexed with ATG017 (PDBID:6SLG, green) and BVD523 (PDBID:6GDQ, light blue) (Ward et al., 2019, Heightman et al, 2018). *Left panel:* Front view showing movement of the Gly loop, helix αC and helix αL16 in an outward direction by BVD523, attributed to the close proximity between the right-side chlorobenzyl substituent and the π orbital of Y34 in the Gly loop (Cl-π distance, 3.3 Å). *Right panel:* View showing left-side hydrogen bonds with main chain atoms of hinge residue M106. **(C)** 2D-HMQC spectra of 2P-ERK2 complexed with ATG017 at 25°C and 5°C, showing [methyl $^{1}H,^{13}C$] peaks of residues I72, L220 and L242. Unlike 2P-ERK2 complexed with BVD523, the ATG017 complex retains R⇌L exchange resembling that of GDC0994 (**Fig. 1**). **(D)** HDX time courses with ATG017 measuring deuterium uptake at the DFG motif, P+1 segment, and helix αF. Time courses for strand β9 are shown in **Suppl. Fig. S8**. Enhanced HDX protection by ATG017 binding is observed at the DFG and adjacent β9 segments, but minimally at the P+1 and helix αF, similar to that seen with GDC0994. The results suggest that allosteric coupling between the ligand binding pocket and distal regions surrounding the activation loop, but not the DFG motif or β9, are characteristic of R-state inhibitors. Structures were superpositioned by aligning Cα atoms within the C-terminal domain (residues 109-141, 205-245, 272-310).

Figure 1

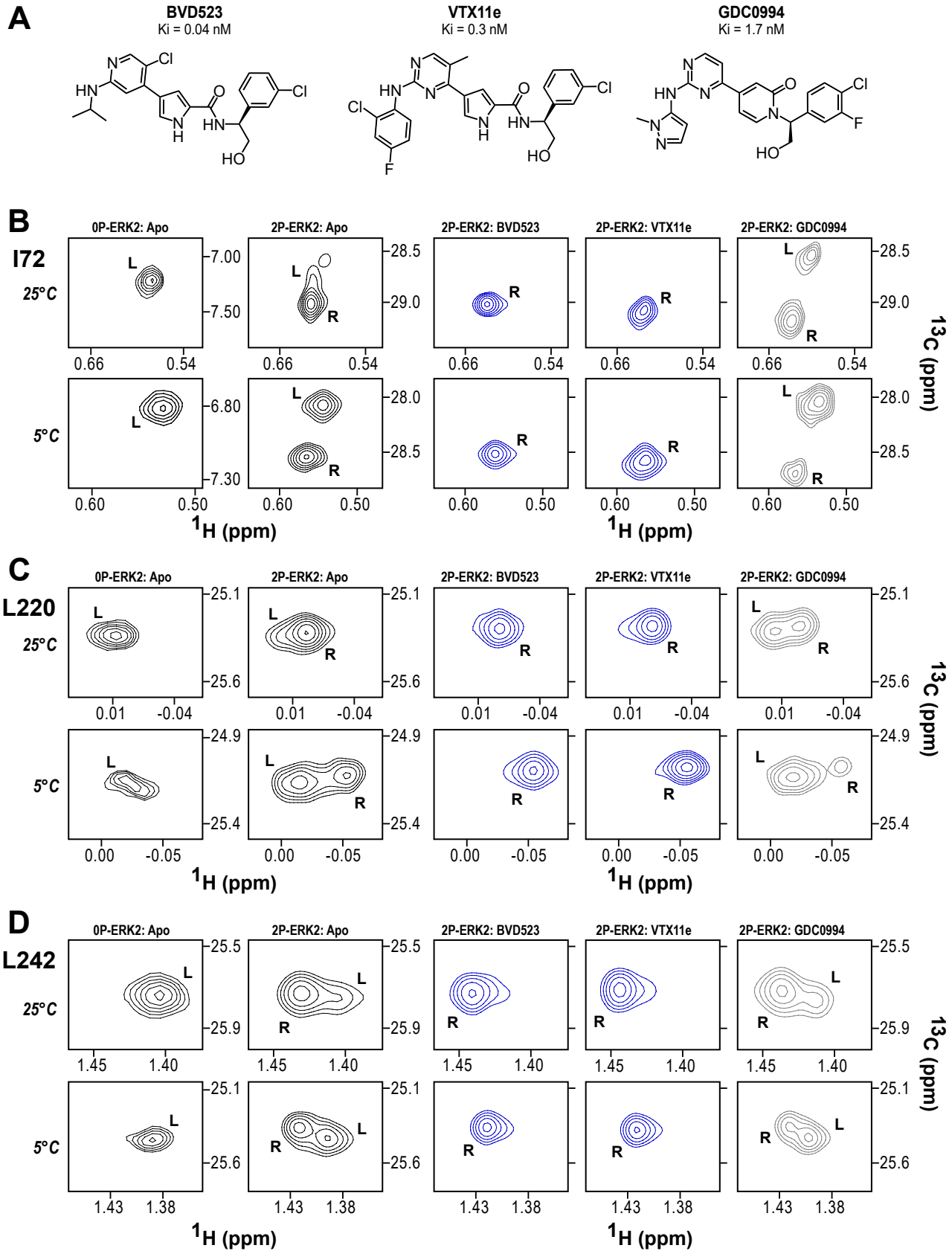

Figure 2

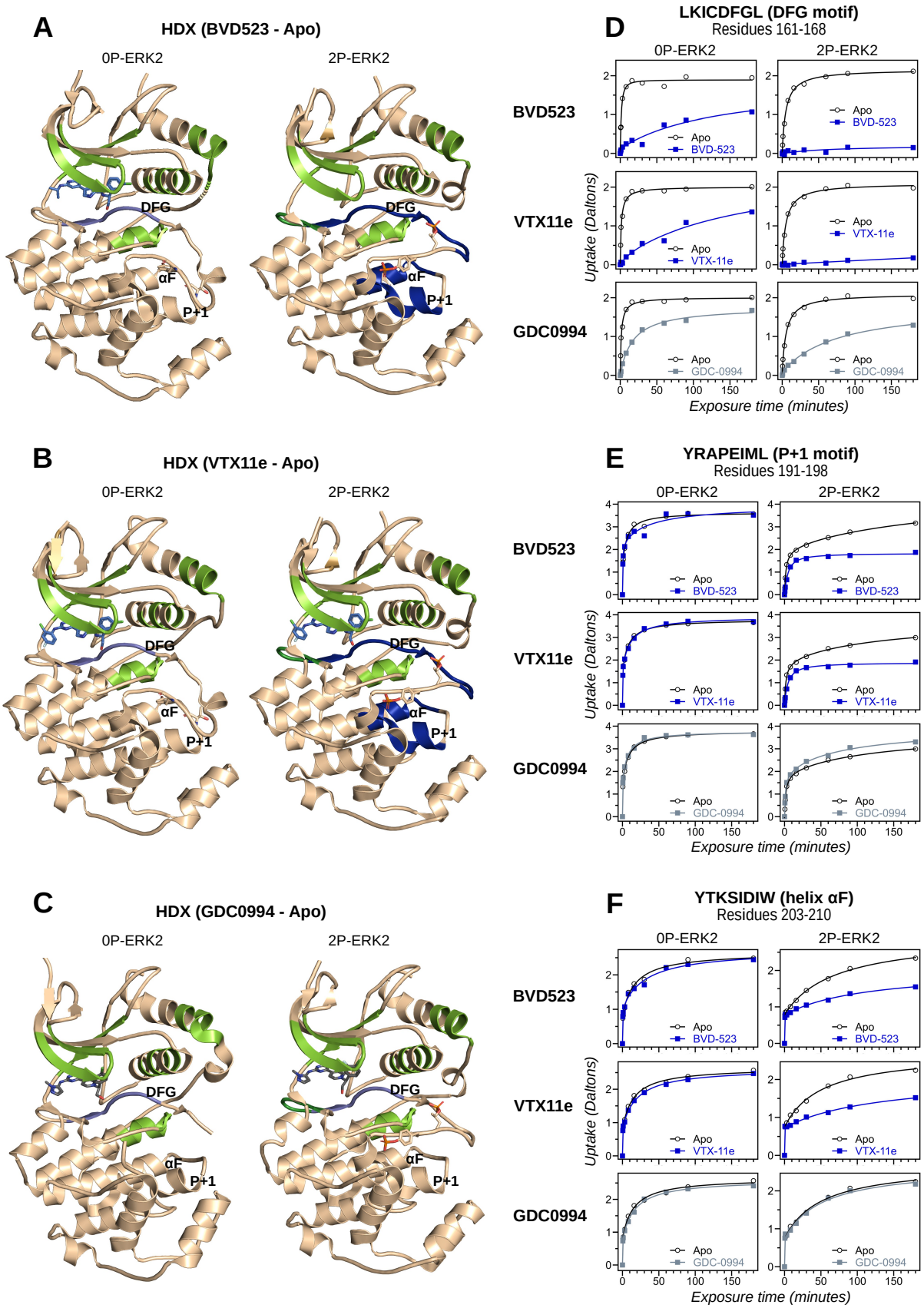

Figure 3

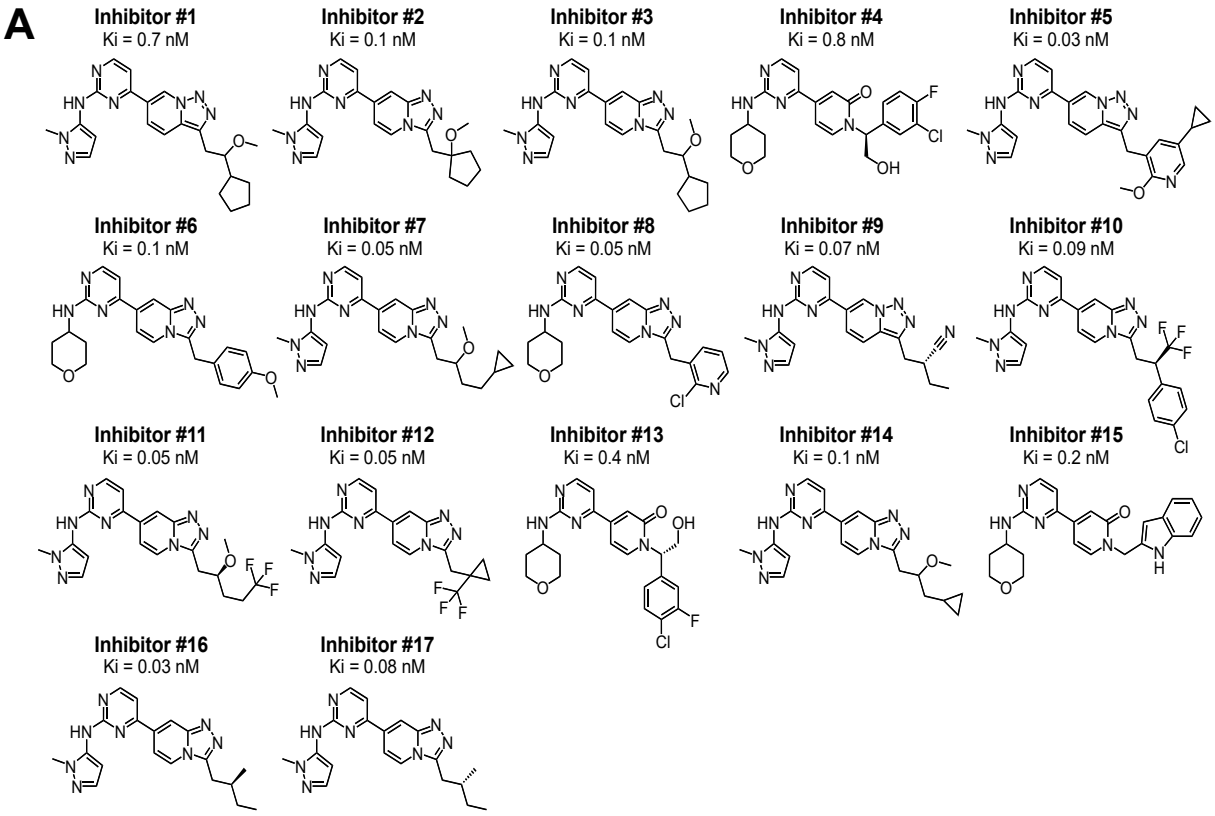

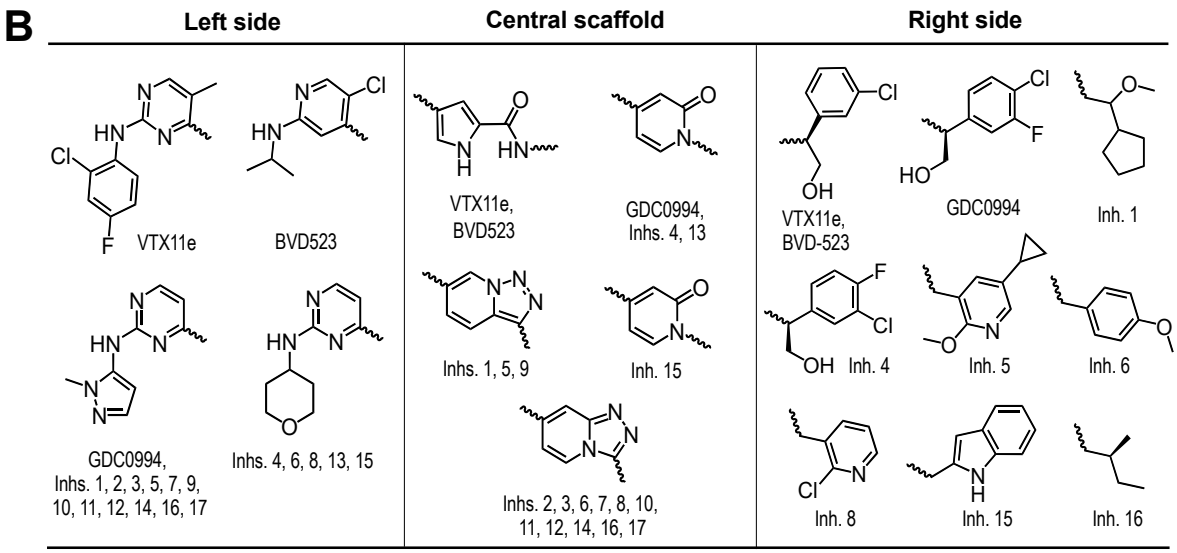

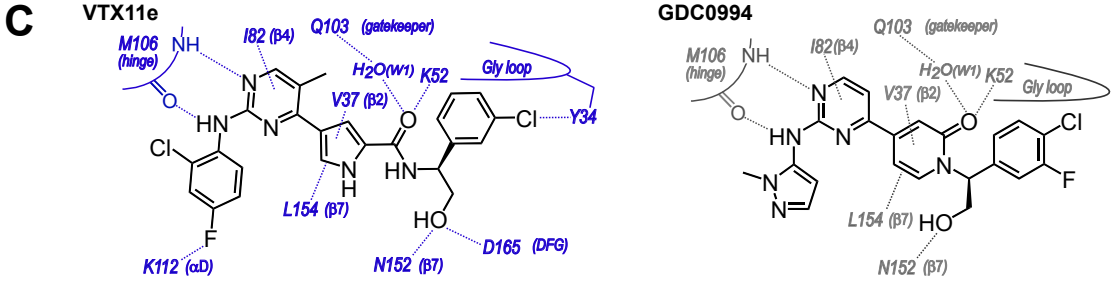

Figure 4

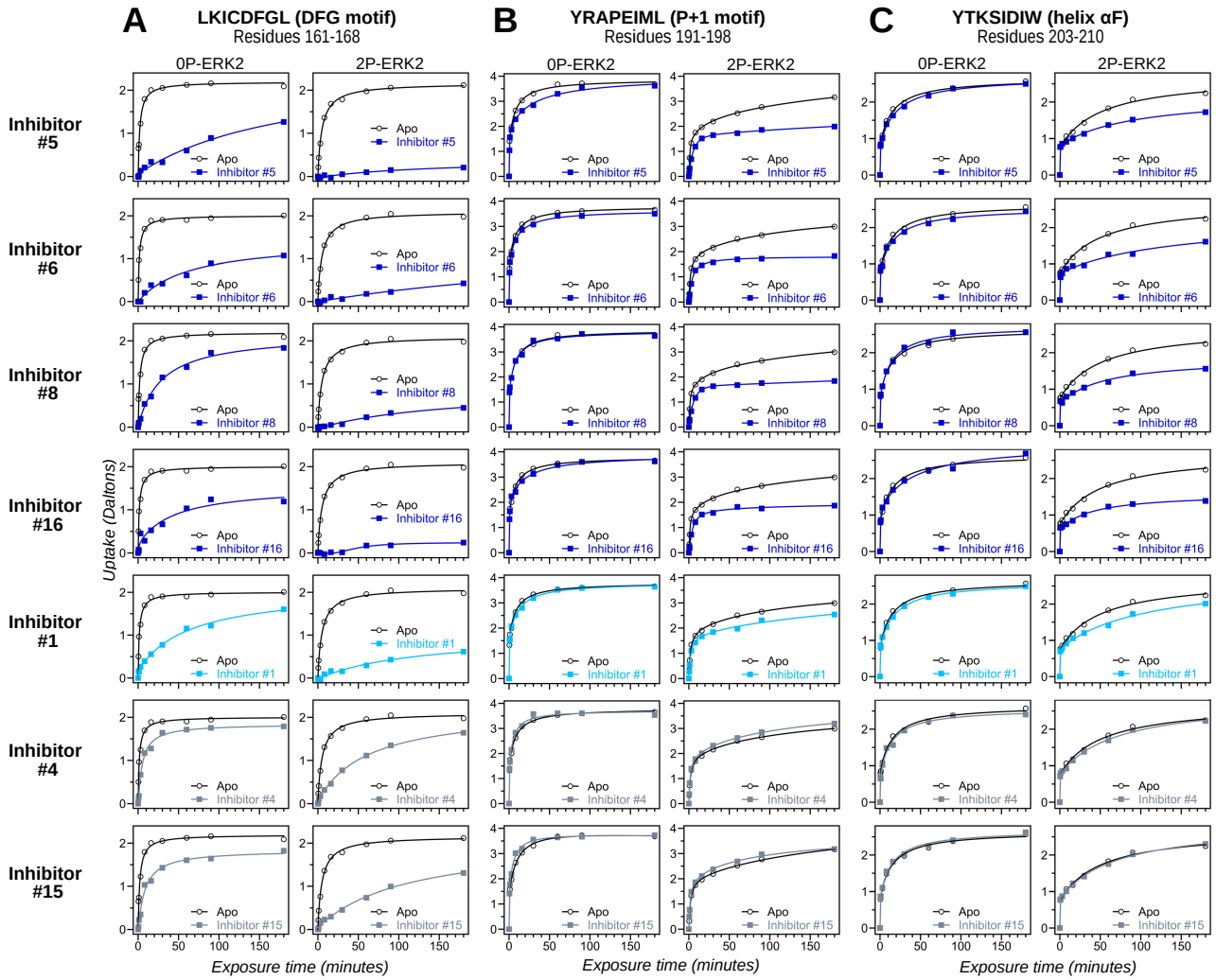

Figure 5

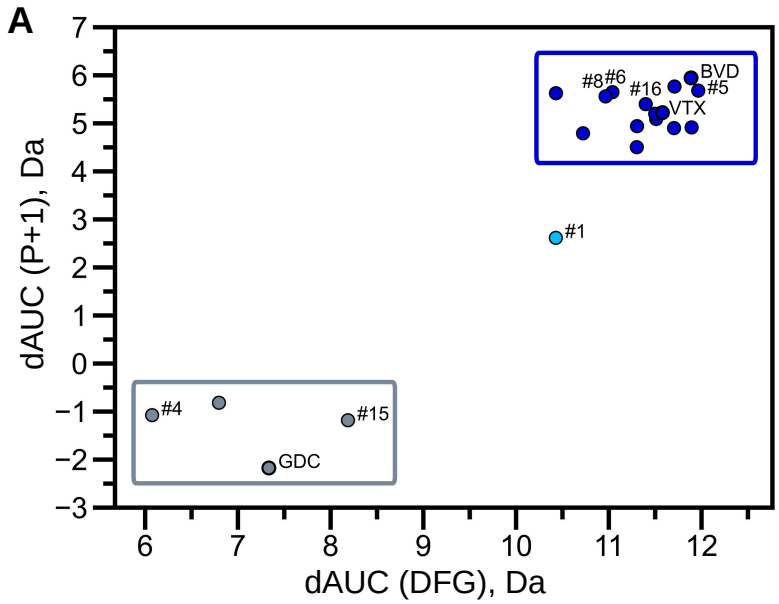

B

Inhibitor	dAUC (Da) DFG	P+1
VTX11e	11.6	5.2
BVD523	11.9	6.0
#5	12.0	5.7
#7	11.9	4.9
#12	11.7	5.8
#11	11.7	4.9
#14	11.5	5.1
#17	11.5	5.2
#16	11.4	5.4
#3	11.3	4.5
#2	11.3	4.9
#6	11.0	5.7
#8	11.0	5.6
#10	10.7	4.8
#9	10.4	5.6
#1	10.4	2.6
#15	8.2	- 1.2
#13	6.8	- 0.8
#4	6.1	- 1.1
GDC0994	7.3	- 2.2

Figure 6

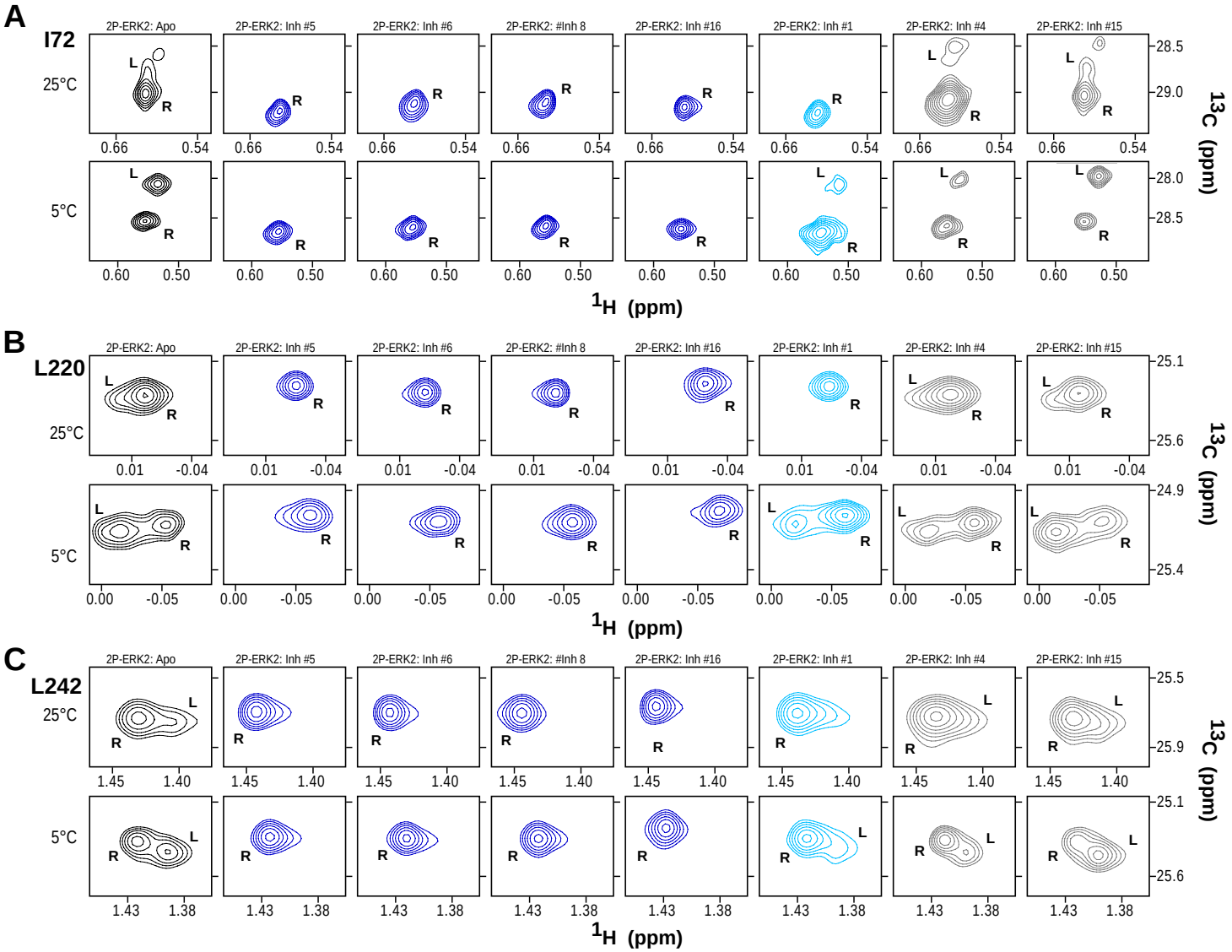

Figure 7

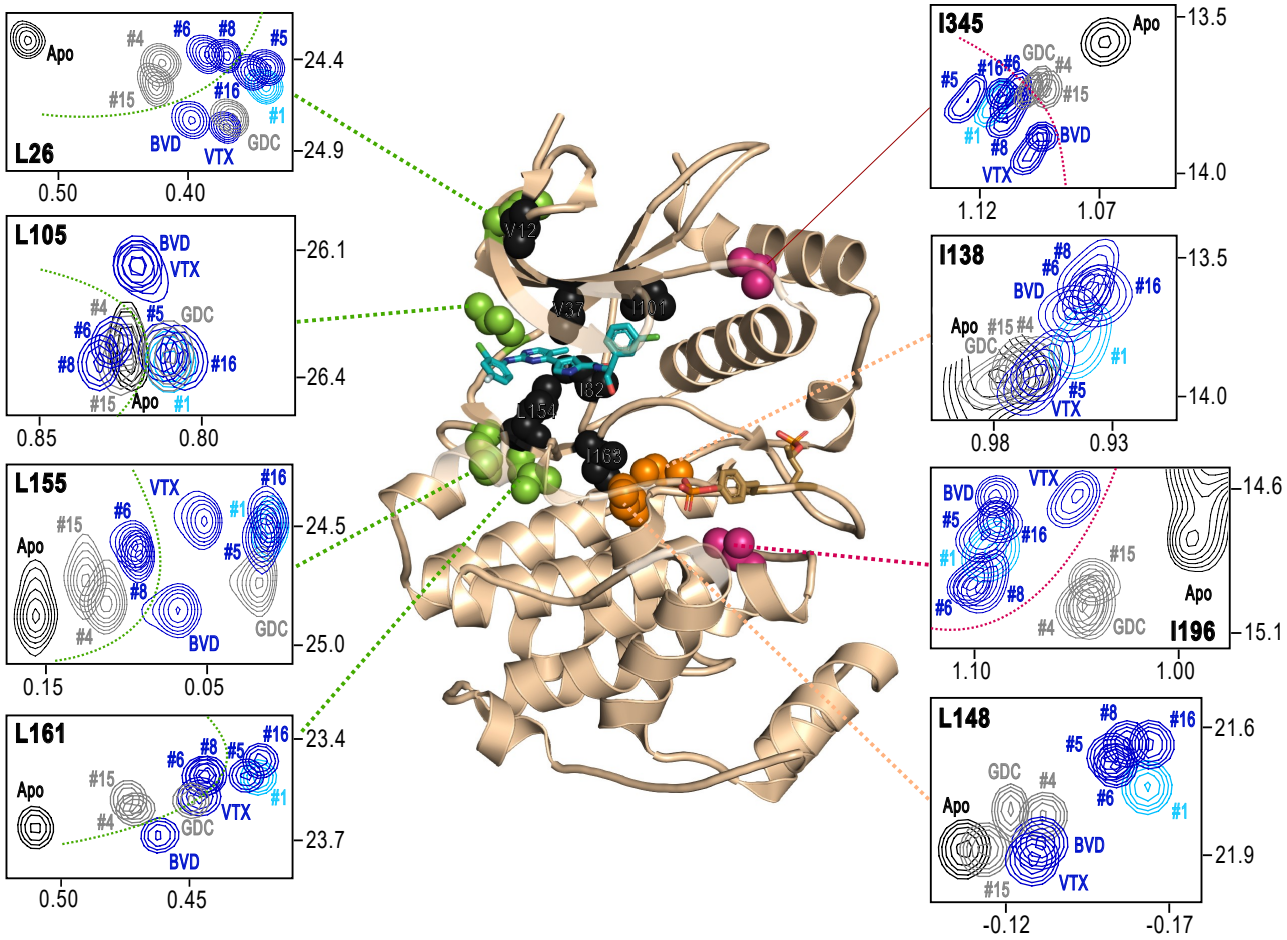

Figure 8

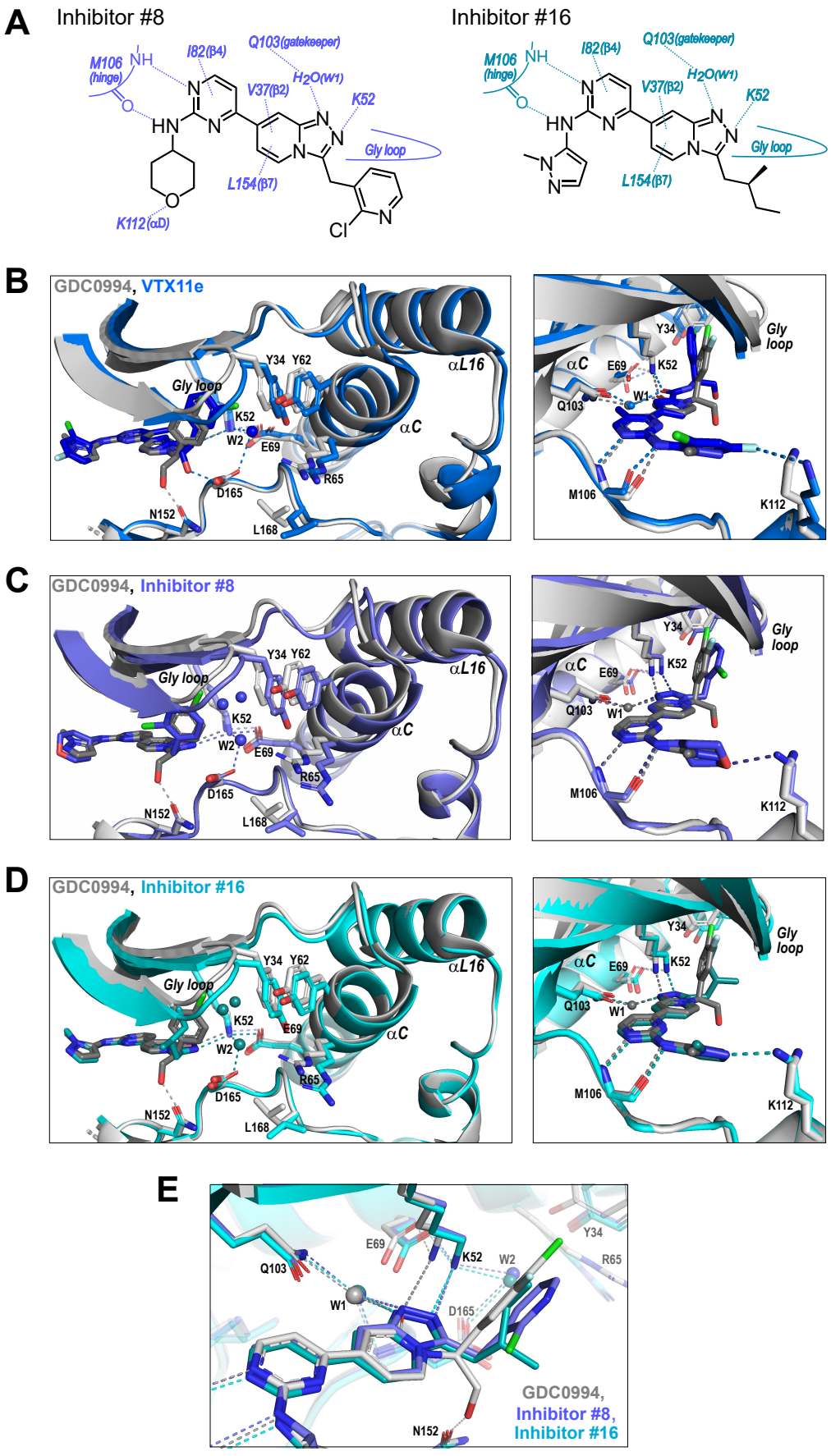

Figure 9